ACS APPLIED NANO MATERIALS

www.acsanm.org Article

Influence of Hard/Soft Layer Ordering on Magnetization Reversal of Bimagnetic Nanoparticles: Implications for Biomedical/Theranostic Applications

Corisa Kons, Kathryn L. Krycka, Joshua Robles, Nikolaos Ntallis, Manuel Pereiro, Manh-Huong Phan, Hariharan Srikanth, Julie A. Borchers, and Darío A. Arena*

Cite This: ACS Appl. Nano Mater. 2023, 6, 10986−11000 Read Online

ACCESS | Metrics & More | Article Recommendations

ABSTRACT: We investigate the spatial distribution of spin orientation in magnetic nanoparticles consisting of hard and soft magnetic layers. The nanoparticles are synthesized in a core−shell spherical morphology where the target stoichiometry of the magnetically hard, high anisotropy layer is $CoFe_2O_4$ (CFO), while the synthesis protocol of the lower anisotropy material is known to produce Fe_3O_4. The nanoparticles have a mean diameter of ∼9.2−9.6 nm and are synthesized as two variants: a conventional hard/soft core−shell structure with a CFO core/FO shell (CFO@FO) and the inverted structure FO core/CFO shell (FO@CFO). High-resolution electron microscopy confirms the coherent spinel structure across the core−shell boundary in both variants, while magnetometry indicates the nanoparticles are superparamagnetic at 300 K and develop a considerable anisotropy at reduced temperatures. Low-temperature *M vs H* loops suggest a multistep reversal process. Small angle neutron scattering (SANS) with full polarization analysis reveals a considerable alignment of the spins perpendicular to the field even at fields approaching saturation. The perpendicular magnetization is surprisingly correlated from one nanoparticle to the next, though the interaction is of limited range. More significantly, the SANS data reveal a pronounced difference in the reversal process of the magnetization parallel to the field for the two nanoparticle variants. For the CFO@FO nanoparticles, the core and shell magnetizations appear to track each other through the coercive region, while in the FO@CFO variant, the softer Fe_3O_4 core reverses before the higher anisotropy $CoFe_2O_4$ shell, consistent with expectations from mesoscale magnetic modeling. These results highlight the interplay between interfacial exchange coupling and anisotropy as a means to tune the composite properties of the nanoparticles for tailored applications including biomedical/theranostic uses.

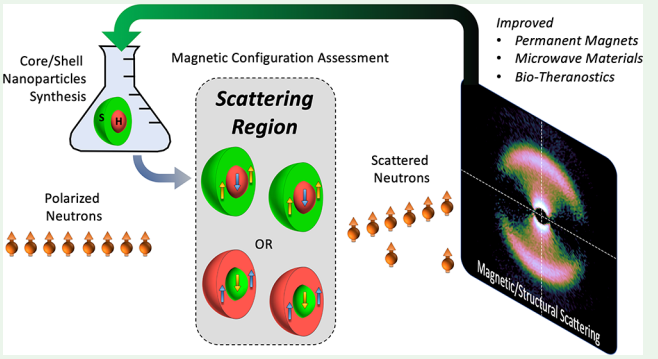

KEYWORDS: *magnetic nanoparticles, core−shell nanoparticles, spinel ferrite, small-angle neutron scattering, polarized neutron scattering*

INTRODUCTION

Magnetic nanoparticles (NPs) are complex systems where unique properties such as enhanced magnetocrystalline anisotropy or variations in the Curie temperature[1−3] can emerge and these can differ greatly when compared to bulk counterparts. Such properties can be further tailored in core−shell NP structures by careful selection of the constituent materials where interfacial coupling plays a strong role in the exchange interaction between layers.[4] Indeed the role of exchange coupling in composite structures containing both soft and hard magnetic phases has been studied extensively over the years as an avenue for tuning magnetic properties (Figure 1).[5−8] Such a method pairs the high anisotropy of a hard magnet with the high moment of the soft material for use in a variety of applications including biomedicine,[9,10] data storage[11] and rare-earth free permanent magnets.[12]

The miniaturization of magnetic systems into the nano-region results in large surface area to volume ratios and, thusly, increases the fraction of surface spins compared to those in the bulk.[13] As such, the sensitivity of the magnetic system to surface contributions becomes crucial and surface effects become driving forces in determining the overall magnetic properties.[14] Surface spin disorder as a result of symmetry breaking in the crystal structure at the NP surface and altered exchange interactions lead to canted spins and a reduction in

Received: February 3, 2023
Accepted: May 26, 2023
Published: June 14, 2023

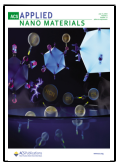

https://doi.org/10.1021/acsanm.3c00510
ACS Appl. Nano Mater. 2023, 6, 10986−11000

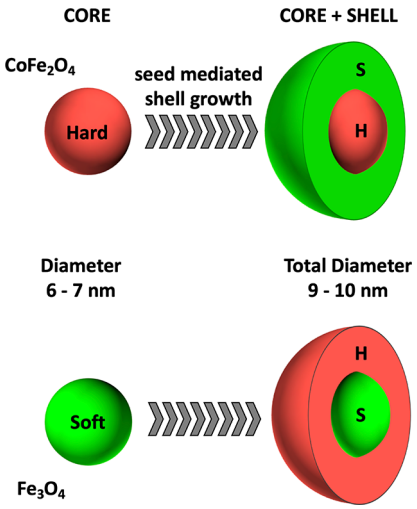

Figure 1. Synthesis of core@shell NPs in hard@soft and soft@hard configurations.

magnetic moment of the NP.[2] In general, surface spins are more susceptible to spin canting than interior moments, and such canting has been observed experimentally in many ferrites and iron oxides NPs.[15−21] The degree of canting is influenced by anisotropy,[22] intraparticle effects due to Dzyaloshinskii−Moriya interactions and NP size[23] allowing for possible ways to tailor spin disorder in core−shell NPs through careful selection of constituent materials and synthesis parameters.

Spinel ferrites of the form MFe_2O_4, where M is a divalent transition metal, are an attractive class of ferrimagnets offering both soft and hard phases as well as a common crystal structure that allows for a high-quality crystal interface between core and shell layers.[24] In such materials the metallic ions are located at either octahedrally (B) coordinated sites or those with a tetrahedral (A-site) geometry and can adopt a normal, inverse or mixed spinel structure.[25] The ferrimagnetic nature of this class of materials arises from the antiparallel alignment of spins on the A and B sites. Of importance to this work is the inverse spinel structure where Fe^{3+} cations are equally distributed at both A and B sites, while the divalent M ions are found only at octahedral sites. In this work, $CoFe_2O_4$ (CFO) was selected due to its high anisotropy that should limit the degree of canting or support uniform spin canting,[26] as the spins will be more tightly bound to the crystal lattice compared to Fe_3O_4 (FO), which has a relatively high moment but much lower anisotropy. A common crystal structure and negligible differences in lattice constant between the two materials (8.40 Å for FO, 8.39 Å for CFO[27]) enables synthesis of high-quality core−shell NPs. The synthesis reaction used to generate the Fe oxide cores or shells in this study is known to produce Fe_3O_4[28], and Fe_3O_4 can retain its signature magnetic, electronic and structural order even after more than 150 days of oxidation at ambient conditions.[29] We note, however, that structurally and magnetically Fe_3O_4 can be difficult to distinguish from the closely related Fe oxide γ-Fe_2O_3. For convenience, we refer to the Fe oxide phase in our core−shell NPs as Fe_3O_4 as this is the most likely phase of Fe oxide in our samples.

Two core−shell NP variants were examined in this study: a conventional one in which the core is high anisotropy $CoFe_2O_4$ and is surrounded by a magnetically softer shell composed of Fe_3O_4 (core@shell, CFO@FO) and the inverted structure (FO@CFO) where the higher anisotropy material is now in the shell. Combinations of hard and soft magnetic materials in quasi-spherical NPs enable optimization of properties for diverse applications including information storage,[30,31] permanent magnets[32] and others. In the biomedical field, magnetic NPs have found use as enhanced contrast agents for magnetic particle imaging[33] and as sources of localized heating of biological tissue.[34,35] Hysteresis losses occurring under high-frequency (AC) excitation are the primary mechanism for localized tissue heating in single magnetic domain NPs such as the bimagnetic NPs in the present study, and guided modification of the size of the AC hysteresis loop area will help promote the development of core−shell NPs for magnetic hyperthermia applications.[36] Hence, developing methods to understand and control parameters such as NP composition, size, morphology, hard layer/soft layer ratio, and interfacial coupling, which directly affect AC magnetic hysteresis losses, is of critical importance.

Although both variants of NPs in this study are composed of the same set of materials (Fe_3O_4 and $CoFe_2O_4$), there are a number of intrinsic factors that may influence the spin arrangement and interfacial coupling. Curvature effects between the two NP variants will be different at the interface for core−shell structures compared to other geometries;[37,38] in the CFO@FO system, the $CoFe_2O_4$ core will have concave curvature at the core−shell boundary, while the Fe_3O_4 shell will see convex curvature that is reversed in the FO@CFO structure. Recent reports have demonstrated the effect of curvature on magnetization in $CoFe_2O_4/Fe_3O_4$ bent heterostructures that may be applicable to core−shell NPs as well.[37] The outermost layer may see differences in surface chemistry or uncompensated spins affecting surface contributions to overall magnetic properties. Such effects can lead to noncollinear spin arrangements or canted layers that inhibit desired magnetic properties as magnetic moments no longer lie parallel to the applied field. The combination of magnetically hard and soft layers can also lead to magnetic proximity effects as the anisotropy of the $CoFe_2O_4$ layer can delay the onset of superparamagnetism (SPM) in the magnetite,[39−42] and generally SPM NPs are favored for biological applications as the absence of remanent magnetization minimizes agglomeration in the absence of external magnetic fields. We also note that while the biocompatibility of magnetite is well-known, there are methods to enhance the biocompatibility of $CoFe_2O_4$.[43−46]

The structural and magnetic systems of each NP variant were explored using a variety of techniques including transmission electron microscopy (TEM), field- and temperature-dependent magnetometry, mesoscale magnetic simulations of NP ensembles, and also fully spin-polarized small-angle neutron scattering (SANS). The latter is a technique capable of providing both structural and magnetic details of the individual core−shell layers as well as interparticle spin correlations with differing length scales and degree of coherence.[47−50] The ensemble average of both the magnitude and direction of magnetic moments can be resolved allowing for differentiation between reduced moments and presence of tilted spins. Field- and temperature-dependent magnetometry were collected and compared to Langevin generated magnetization curves as such methods can also provide evidence of tilted spins in the NPs. Mesoscale magnetic simulations were also performed to discern the mechanisms responsible for tilting of spins in each $CoFe_2O_4/Fe_3O_4$ NP variant.

https://doi.org/10.1021/acsanm.3c00510
ACS Appl. Nano Mater. 2023, 6, 10986−11000

The paper is organized as follows: results of imaging, magnetometry and magnetic simulations are presented in the following subsection. Reduced SANS data and results of multiscale modeling of the neutron scattering are presented in the subsequent subsection. We conclude the main part of the manuscript with a discussion and conclusions regarding the results and analyses. Methods for the sample synthesis, experimental and numerical simulation methods, and reduction and modeling of scattering data are contained in the final section.

RESULTS AND ANALYSIS

Nanoparticle Imaging and Magnetic Studies. CFO@FO and FO@CFO NPs were synthesized using a seed mediated thermal decomposition process. Transmission electron micrographs (TEM) presented in Figure 2 indicate that each $CoFe_2O_4/Fe_3O_4$ core−shell variant is primarily spherical but with faceting showing 6-fold symmetry. Due to the low Z-contrast between $CoFe_2O_4$ and Fe_3O_4 and shell layers close to the minimum resolution of the TEM, it is not possible to see the individual core−shell layers. Lattice fringes are coherent across the core−shell structure indicating a coherent structure. Note also that the NPs themselves appear to be close packed, suggesting that a significant fraction of the NPs locally self-assemble upon drying.

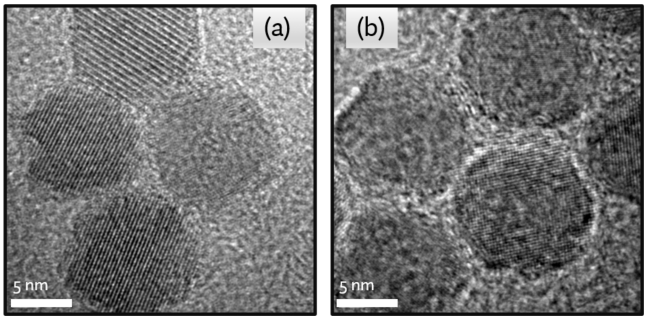

Figure 2. HR-TEM images for the NPs used in the neutron scattering study of (a) CFO@FO and (b) FO@CFO core−shell NPs confirm the spherical shape and overall size. Owing to the thin shell and similar material densities between the core and shell layer, it is not possible to see the individual NP layers with TEM.

Temperature- and field-dependent magnetometry scans were collected for each NP ensemble; Figure 3 shows hysteresis loops at 5 and 100 K along with field-cooled (FC) and zero-field-cooled (ZFC) M vs T curves for CFO@FO and FO@CFO. Field cooling and other temperature-dependent magnetometry were performed in a 10 mT field for all measurements. Note that mass normalization contains contributions from organic surfactants that coat the NPs and we estimate the surfactants contribute between 2% to 4% of the total mass. From Figure 3b,d it can be seen that the blocking temperature for the CFO@FO NPs is well above room temperature, whereas the FO@CFO NPs have a blocking temperature of ≈275 K. The hysteresis loops at 5 and 100 K confirm the ferrimagnetic nature of both NPs below the blocking temperature with coercivity increasing as temperature decreases.

Hysteresis loops at 5 and 100 K in Figure 3a for CFO@FO NPs have similar saturation moments of 86 Am^2/kg and both show a secondary structure, or knee-like feature, between 0 and 1 T, suggesting a more complex spin reversal process between the core and shell. In the FO@CFO NPs, this step is only present in the 5 K hysteresis loop as seen in Figure 3c, while the 100 K loop shows no inflection at low fields; the saturation values for the FO@CFO NPs are considerably different too, about 63 Am^2/kg at 100 K and increasing to 80 Am^2/kg at 5 K.

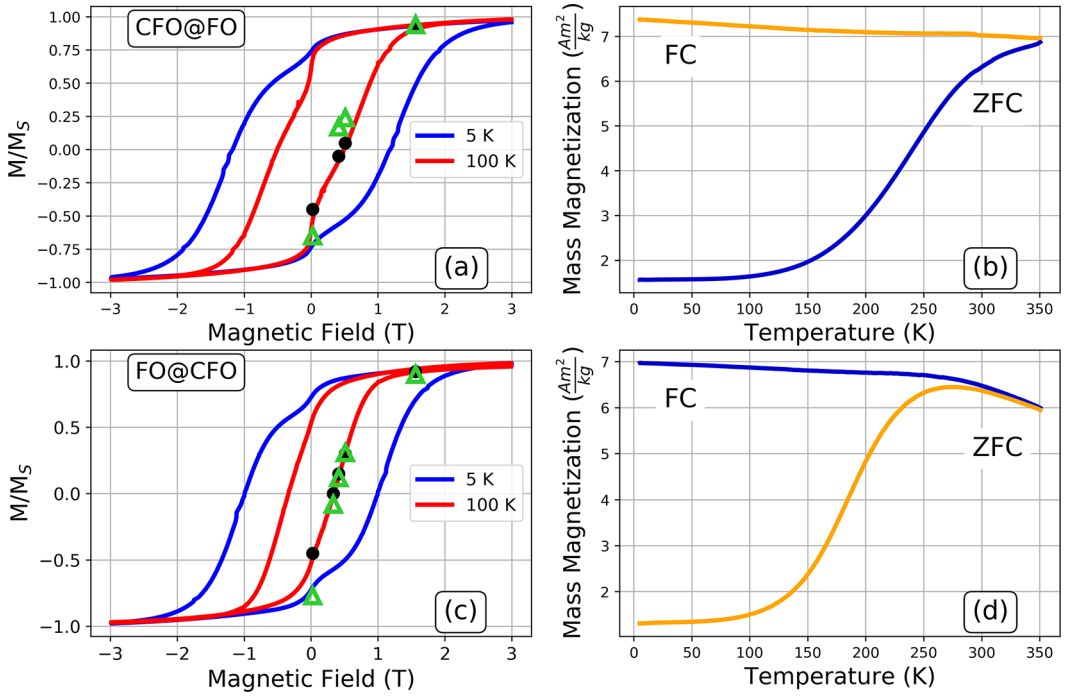

Figure 3. Magnetization vs applied field curves at 5 and 100 K for (a) CFO@FO and (c) FO@CFO NPs with the corresponding FC and ZFC M vs T curves shown to the right for each NP (b,d). In (a,c), black dots indicate fields where SANS measurements were performed at 100 K. Green triangles are mSLDs from SANS analyses, scaled to M_s.

https://doi.org/10.1021/acsanm.3c00510
ACS Appl. Nano Mater. 2023, 6, 10986−11000

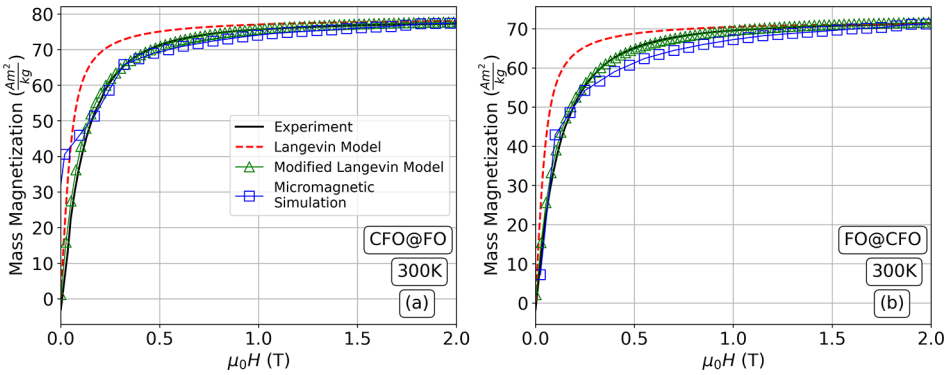

Figure 4. Magnetization curves for (a) CFO@FOand (b) FO@CFO at room temperature (black lines). Also shown are the field magnetization profiles extracted from the bare Langevin function (eq 1, red dashed line), the modified Langevin model (refs 51−53), green triangles, and the mesoscale magnetic simulation (blue squares).

Table 1. Heisenberg Interaction Constant J_{ij} for the Macrospin Model[a]

NP Variant	J_{12}	J_{13}	J_{23}	J_{24}	J_{34}	J_{25}	J_{35}	J_{45}	J_{46}	J_{56}
CFO@FO	3.4	3.4	−2.1	2.3	1.9	2.2	1.8	2.4	2.4	−1.8
FO@CFO	3.1	3.1	−1.8	2.1	2.2	2.3	1.7	2.8	2.8	−1.9

[a]All J_{ij} are in units of mRy. Vertical lines distinguish interactions within the core alone, between the core and shell, and solely in the shell.

The two NP variants also exhibit differences in coercivity indicating changes in exchange coupling based on the selection of hard or soft materials in the core and shell. At 5 K, when magnetically hard $CoFe_2O_4$ is in the core and paired with a softer Fe_3O_4 shell, there is a coercive field ∼1.3 T (Figure 3a), while the inverted variant (FO@CFO) has a smaller coercive field of ∼1 T (Figure 3c).

Reflecting the lower blocking temperature, the FO@CFO NPs are superparamagnetic (SPM) at room temperature while CFO@FO NPs have a small coercive field of ≈6 mT and remnant magnetization on the order of 3.5 Am^2/kg. Since both NP samples were in or very near the SPM state, the magnetic response can be approximated using a Langevin function $\mathcal{L}(x)$ of the following form to simulate the $M(\mu_0 H)$ curves:

$$M(\mu_0 H) = n\mu\mathcal{L}\left(\frac{\mu_0 H\mu}{k_B T}\right), \quad \text{where } \mathcal{L}(x) = \frac{1}{\tanh(x)} - \frac{1}{x} \tag{1}$$

where n is the total number of particles, μ is the magnetic moment per particle (Am^2), $\mu_0 H$ is the applied field (T), k_B is the Boltzmann constant, and T is temperature.[18] A value of μ was assigned for each NP based on core radii and shell thicknesses determined from modeling of the SANS data (see below) and M_S derived from experimental $M(H)$ curves shown in Figure 4. In both NPs, there are deviations between the experimental data and Langevin generated hysteresis loops below 0.8 T for CFO@FO NPS and 0.7 T for FO@CFO variants. If uniform magnetization is assumed for each NP in eq 1, then the experimental values for μ would describe magnetic correlations at high and low fields. Near 0.1 T each NP sees a ≈25% reduction in the experimental moment compared to the Langevin model indicating a reduction in the parallel magnetic component at low fields likely as a result of spin canting or spin disorder in a direction perpendicular to the field.[18]

The bare Langevin analysis assumes a uniform total moment per particle, while TEM imaging and structural neutron scattering (below) indicate a variation of particle size and hence of moment per particle. We also display in Figure 4a modified Langevin model that includes a log-normal distribution of NPs (green triangles).[51−53] The agreement with the measured M vs H curve is improved considerably, particularly in the low field region. For the FO@CFO system (Figure 4b), the magnetic diameter from the modified Langevin approach is 7 ± 2 nm (1σ), while the magnetic diameter of the inverted CFO@FO variant comes in at 7 ± 1 nm. This is considerably smaller than the apparent size in the TEM images in Figure 2 and also smaller than the NP size estimates derived from the structural neutron scattering below. One possible reason is that even at 300 K the particles are not completely in a superparamagnetic state, which is a fundamental assumption of both the Langevin and modified Langevin approaches. Indeed, the CFO@FO NPs exhibit a small coercivity at 300 K of nearly 6 mT, which may be expected as the blocking temperature for these NPs is above room temperature (cf. Figure 3b). Another possible contribution is spin canting or spin disorder in the near-surface region of the NPs, which would tend to reduce the volume of the nearly single domain core region.

To more closely capture the low field behavior of the NP assemblies and also introduce some degree of noncollinearity in the spin distribution across the NP, in Figure 4 we also present calculations from mesoscale simulations of the 300 K M vs H loops. In these simulations, the magnetic behavior of each NP is modeled as six macrospins, three for the core and three for the shell. In addition to anisotropy and Zeeman contributions, the Hamiltonian includes intraparticle interactions between the macrospins, angular-dependent dipolar energies between the total magnetization of different NPs, and Heisenberg interactions between NPs. Please refer to the Methods section and ref 54 for a more complete description of the model.

Tables 1 and 2 present the parameters used for the macrospin model. For the different NPs, indices {1−3} refer to the core and {4−6} to the shell. In all cases, the anisotropy was assumed to be uniaxial for each particle, and its axis was randomly selected per particle in the assembly. J_{inter} was set to

https://doi.org/10.1021/acsanm.3c00510
ACS Appl. Nano Mater. 2023, 6, 10986−11000

Table 2. Anisotropy Constant k for the Macrospin Model[a]

NP Variant	k_1	k_2	k_3	k_4	k_5	k_6
CFO@FO	7.1	13.1	13.1	8.1	7.6	0.1
FO@CFO	0.8	6.4	6.4	9.2	8.1	8.0

[a]All k are in units of mRy. k_1 through k_3 simulate the core, while k_4 through k_6 correspond to the shell.

0.2 mRy. To reduce the number of free parameters fit, one of the three macrospins assigned per material, index {1} for the core and index {4} for the shell, is restricted to interact with the same exchange strength with the other two macrospins of the same material (i.e., $J_{12} = J_{13}$ and $J_{45} = J_{46}$, see Table 1). In this regime there are two exchange constants per material that have to be tuned. Table 2 presents the anisotropy constants used in the model, which highlight the difference in anisotropy between the $CoFe_2O_4$ and Fe_3O_4. Generally, one of the Fe_3O_4 macrospins exhibits a much smaller anisotropy: 0.1 mRy for k_6 in CFO@FO and 0.8 mRy for k_1 in FO@CFO. The other two Fe_3O_4 macrospins require a larger anisotropy to match the field hysteresis loops, and these higher anisotropy Fe_3O_4 macrospins represent the Fe_3O_4 macrospins moments, presumably at the core−shell interface, that couple with the harder $CoFe_2O_4$ material. In both cases, the hard/soft interface acts as a strong pinning center which give rise to the large coercive field measured at low temperatures.

The mesoscale calculations (blue squares in Figure 4) present better agreement with the magnetometry data than the bare Langevin approach, particularly for the FO@CFO variant where the superparamagnetic nature of the NPs at room temperature is recovered and the approach to saturation is more gradual than the Langevin model. The multiple macrospins per NP permit a simulation of spin canting that can arise in the NPs, which is consistent with the observation of perpendicular spins in the magnetic SANS data below. A similar slow approach to saturation is recovered for the CFO@FO variant, but the mesoscale model suggests a weak coercivity (nonzero remanence) which is not observed in the 300 K data. Additional details on calculations of the temperature-dependent, ensemble-averaged magnetization, along with a fully atomistic calculation of the spins from a single NP, are presented in ref 54.

Small Angle Neutron Scattering. Neutron scattering data were collected at temperatures ranging from 5 to 300 K and a variety of fields from 0−1.56 T to probe the magnetic configurations in the vicinity of the knee-like feature seen in the hysteresis loops (refer to Figure 3a,c). The experimental configuration utilized a polarized incident neutron beam (either up spin ↑ or down spin ↓) along with polarization analysis of the scattered beam, resulting in four combined cross sections (↑↑, ↓↓, ↑↓, and ↓↑). Representative 2D scattering distributions are shown in Figure 5. In Figure 5a, the sum of the non spin-flip (NSF) scattering cross sections (↑↑ + ↓↓) is nearly isotropic with angle (θ) relative to a field applied along the X-direction and reflects the dominant nuclear (structural) scattering. In particular, the bright ring located about halfway out in momentum transfer ($|Q|$) corresponds to Bragg diffraction scattering from coherent regions where the NPs assemble into close-packed structures. The logarithmic color scale used obscures any difference in intensity between scattering along the field direction (X-axis, $\theta = 0°$) and the structural + magnetic scattering at $\theta = \pm 90°$. However, in Figure 5b, the difference between the non spin-flip neutron distributions (↓↓ − ↑↑) reveals the scattering asymmetry caused by the magnetization of the NPs. Refer to the Methods section for additional details on the experimental configuration.

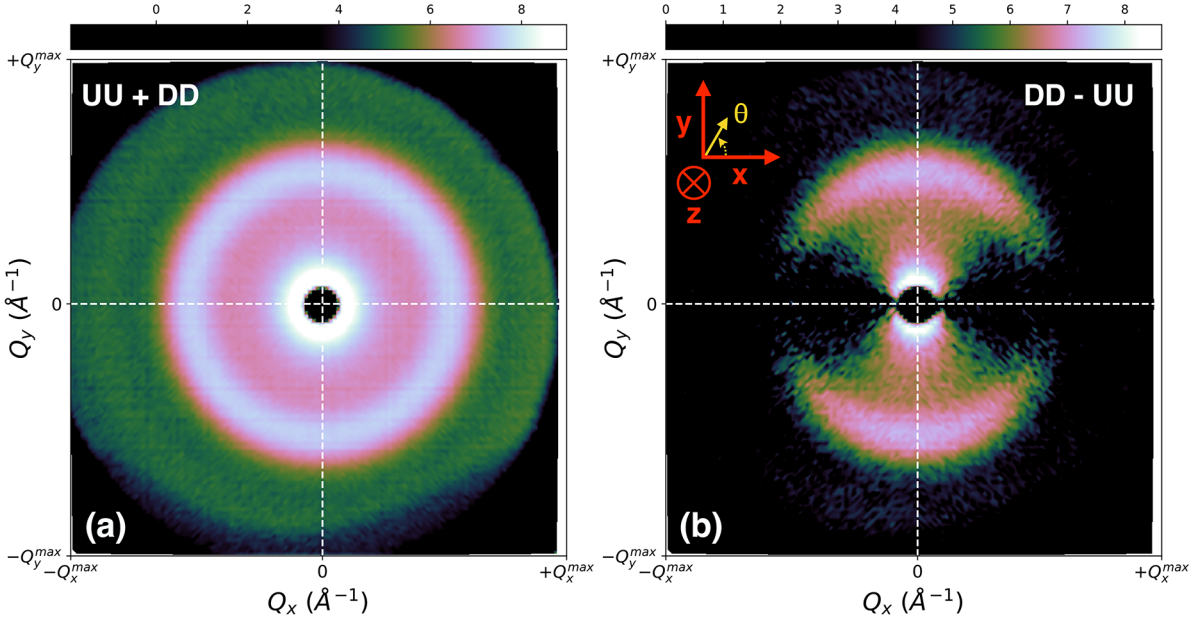

Figure 5. Representative 2D scattering distributions for FO@CFO NPs in a 1.56 T field at 100 K for (a) sum of non spin-flip scattering (↑↑ + ↓↓) and (b) difference of non spin-flip scattering (↓↓ − ↑↑). Panel (b) also presents the coordinate system for these measurements. Note that intensities have been normalized, and both scattering distributions are plotted in a logarithmic color scale with a threshold to suppress low count pixel noise. In panel (a), the structural diffraction peak is evident as a bright ring located away from $Q_{x,y} = 0$, while in the difference distribution (b), the magnetic scattering is evident as the bright regions at $\theta = \pm 90°$, where θ is the azimuthal angle relative to the x-axis. In both panels, $|Q_{x,y}^{max}| \approx 0.13$ Å^{-1} for the detector setting used. Sector cuts of the non spin-flip and spin-flip cross sections at $\theta = 0°$, 180° and $\theta = \pm 90°$ for different fields are used to extract out the nuclear and magnetic scattering; see eqs 3−6 in the Methods section.

https://doi.org/10.1021/acsanm.3c00510
ACS Appl. Nano Mater. 2023, 6, 10986−11000

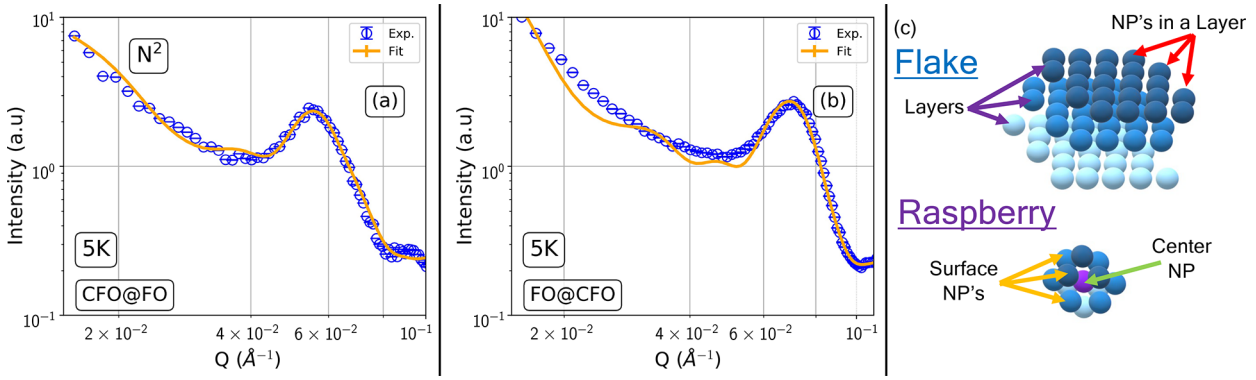

Figure 6. SANS nuclear (N^2) intensities for each CS NP variant as a function of the scattering vector Q at 5 K under HF (1.56 T) conditions. The solid lines show the best fit for each NP using a core + multishell model. Nuclear components were calculated as described in eq 3 in the Methods section using ±10° sector averages of the 2D data. In panel (c), a schematic of the model used in the structural and magnetic fits is presented. The "flake" component considers scattering from layers of close-packed core−shell NPs and where the layers are stacked to form a flake. In the "raspberry" model we consider scattering from a central core−shell NP which is surrounded by a cage of surface core−shell NPs.

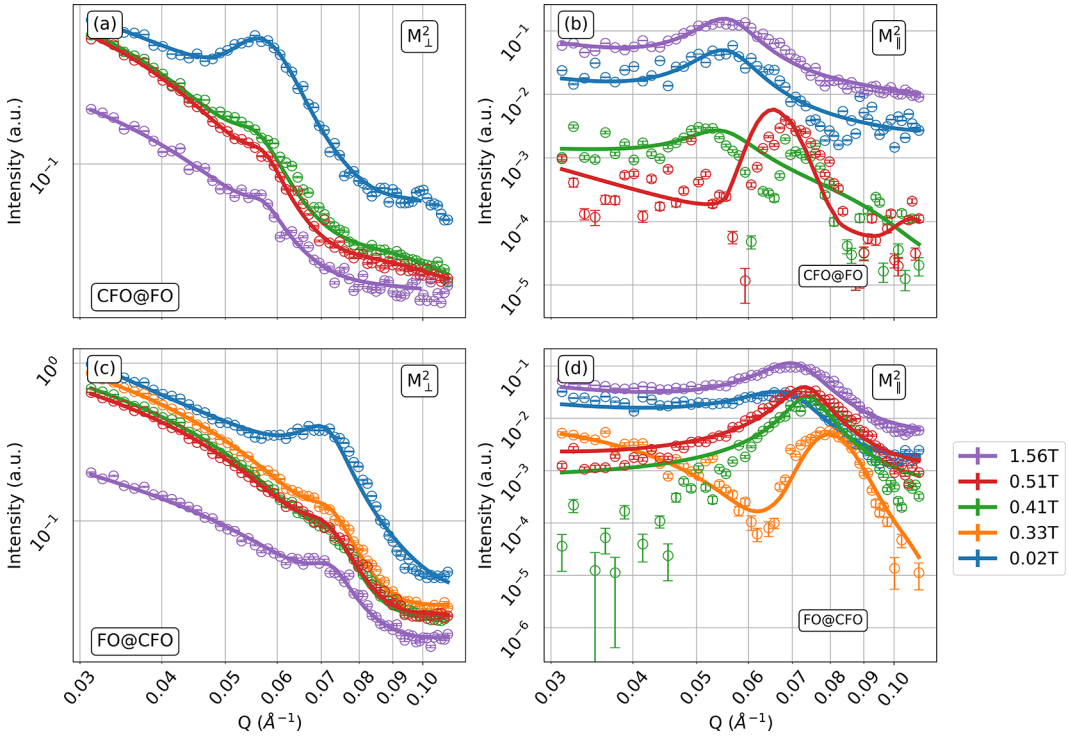

Figure 7. Magnetic SANS data and fits for each core−shell NP variant as a function of the scattering vector Q for 100 K and a variety of applied magnetic field conditions. Open circles represent experimental scattering data while solid lines show the best fit. Panels (a) and (b) present the magnetic SANS data and fits for the CFO@FO NPs; data and fits for the FO@CFO variant are exhibited in panels (c) and (d). $M_\perp^2$ is presented in the left column (a,c) and $M_\parallel^2$ is in right column (c,d). Note the logarithmic scales for the axes.

Each sample was cooled in zero field between temperatures, as the FC M vs T curves showed negligible changes in magnetization at lower temperatures. To reduce random alignment of spins, prior to each SANS measurements the samples were magnetically trained by first saturating the samples to positive saturation, reversing the field direction to negative saturation, back to zero field, and then measuring SANS patterns at the desired positive field values.

Structural parameters were determined by fitting the nuclear scattering; representative experimental data and fits at 5 K are shown in Figure 6 on a semilog scale for each core−shell NP variant. Error bars representing $1-\sigma$ distributions are shown in blue but are typically smaller than the marker size. As suggested by TEM micrographs, the narrow size distribution of each NP type results in a well-defined diffraction peak that reflects the spacing between the NPs in a close-packed structure. In CFO@FO NPs this diffraction peak is centered around $Q \approx 0.055$ Å^{-1} for all temperatures and fields while scattering of the inverted variants reveal a peak near ~0.07 Å^{-1}. The consistency in peak location and width indicates no structural changes for both NP samples with varying field or temperature conditions.

Modeling of the SANS data suggested contributions to the scattering intensity originating from both a finite close-packed ensemble of NPs, referred to as a "flake" which gives rise to a relatively strong diffraction peak, and less coherently ordered

https://doi.org/10.1021/acsanm.3c00510
ACS Appl. Nano Mater. 2023, 6, 10986−11000

Table 3. Fitted Magnetic Scattering Length Density (mSLD) Values in Units of $10^{-6} \times Å^{-2}$ for Core and Shell Layers of Each NP Variant at 100 K[a]

	CFO@FO				FO@CFO				
	0.02 T	0.41 T	0.51 T	1.56 T	0.02 T	0.33 T	0.41 T	0.51 T	1.56 T
$M_{\parallel}^2$									
Core	−0.63	0.31	0.41	1.42	−0.70	0.37	0.70	0.92	0.92
Shell	−1.11	0.23	0.35	1.42	−0.45	−0.37	−0.42	−0.30	0.45
Outer Shell	–	–	–	–	−0.30	−0.27	−0.20	−0.20	0.30
$M_{\perp}^2$									
Core	1.43	0.66	0.57	0.41	1.29	0.69	0.58	0.58	0.40
Shell	1.63	0.81	0.77	0.53	0.86	0.69	0.58	0.58	0.40
Outer Shell	–	–	–	–	0.58	0.59	0.49	0.50	0.17

[a]These fitted mSLD values include additive contributions from the hexagonal flake and raspberry models, though the percentage of each varies with field, as discussed in the text. Note that the changes in the relative scaling among the contributions from the hexagonal flake and raspberry models (refer to Methods section), which were used to model the structural and magnetic scattering, may introduce overestimates of the $M_{\perp}^2$ values (e.g., 0.02 T). The field-dependent trends, however, are robust. For comparison the mSLD values for bulk materials is 1.42 for $CoFe_2O_4$ and 1.46 for Fe_3O_4.

NP structures referred to as "raspberries" that contribute to scattering intensity at lower momentum transfer. Refer to Figure 6c and the Methods section for additional details. For the CFO@FO variant, fitting results gave an estimated average overall NP diameter of 9.2 ± 0.15 nm with a $CoFe_2O_4$ core radius of 2.9 ± 0.03 nm and a Fe_3O_4 shell thickness of 1.7 ± 0.03 nm. The inverted (FO@CFO) variant had a similar overall NP diameter of 9.6 ± 0.3 nm but different core and shell dimensions; the Fe_3O_4 core had a larger radius at 3.5 ± 0.05 nm; the CFO layer was divided into two sublayers for consistency among structural and magnetic fits with a first CFO layer that is 0.8 nm thick and a second outermost layer that is 0.5 nm thick with reduced neutron scattering length density (SLD). In CFO@FO NPs the average core−shell volume fraction is calculated to be V_C/V_S = 0.34 while the inverted FO@CFO structure with a slightly larger core sees an increase in the core−shell volume fraction to about ≈0.63.

Material compositions were confirmed with the model by comparing fitted SLD values to known values for $CoFe_2O_4$ and Fe_3O_4. Fitted SLDs for $CoFe_2O_4$ in the core were found to be 5.6 ± 0.1 × 10^{-6} $Å^{-2}$, which is within 10% of the theoretical SLD (6.07 × 10^{-6} $Å^{-2}$)[55] and matches well with reported values from similar NP systems.[56,57] To accurately capture the evolution of the magnetic scattering (below), the model for the FO@CFO NPs divides the CFO layer into two concentric shells with slightly varying scattering parameters. In this model, the SLD of the inner shell is 5.5 ± 0.2 × 10^{-6} $Å^{-2}$ (again, within 10% of expected values), and the inner shell is surrounded by a narrow, 0.5 nm thick outer CFO shell with a reduced SLD of 2.2 ± 0.2 × 10^{-6} $Å^{-2}$. This outer shell with reduced SLD may indicate a narrow (∼half a unit cell), more porous $CoFe_2O_4$ layer near the surface of the NP. Larger variations in SLDs are observed for Fe_3O_4; when Fe_3O_4 comprises the core in the FO@CFO NPs, the estimated SLD is 6.9 ± 0.1 × 10^{-6} $Å^{-2}$, close to the bulk value of 6.97 × 10^{-6} $Å^{-2}$, while the SLD estimate drops to 5.9 ± 0.1 × 10^{-6} $Å^{-2}$ when Fe_3O_4 forms the shell of the CFO@FO NPs. For both CFO@FO and FO@CFO, analyses of the SANS structural (nuclear) scattering cross sections indicate a reduction of the SLD in the outer layers of the NPs, possibly from an increase in porosity or other form of structural variation near the surface of the NPs.

A fully polarized SANS setup provides the capability to probe the 3D magnetic structure of NPs at variable fields allowing for determination of spin alignment.[58] Representative calculations of parallel ($M_{\parallel}^2$) and perpendicular ($M_{\perp}^2$) magnetic scattering cross sections from spin selection rules, where ∥ and ⊥ represent the orientation of the moments relative to the field, are summarized in eqs 4 and 5 in the Methods section; these data are presented in Figure 7 where changes in scattering shape and intensity with field can be observed. A common story emerges for perpendicular spins ($M_{\perp}^2$) of both NP variants (Figure 7a,c); at low field a well-defined magnetic diffraction peak is present. For both the CFO@FO and FO@CFO NPs the perpendicular magnetic diffraction peaks overlap with those from nuclear scattering indicating this spin alignment persists over a collection of NPs in the assembly. The perpendicular alignment is uniform within each NP and is correlated from one particle to the next.

The $M_{\parallel}^2$ magnetic scattering contribution is representative of the net scattering between magnetic moments aligned both antiparallel and parallel to the applied field. Figure 7b shows parallel spin ordering for CFO@FO NPs at various fields; a weak diffraction peak is observed at 0.02 T after application of a −1.56 T field. However, as the field is increased near the coercive field ($\mu_0 H_C$ = 0.41 T), parallel magnetic ordering collapses with diffraction peaks that are not well-defined, starts to reorder just above the coercive field (0.51 T) at higher Q, and comes back strongly at high field (1.56 T). Parallel scattering in FO@CFO NPs, shown in Figure 7d, indicates a more complex spin ordering process; a diffraction peak develops at low field (0.02 T), but as the field is increased to near (0.33 T) and slightly above coercivity (0.41 T, and 0.51 T), the diffraction peaks shift to higher Q values until the highest applied field (1.56 T) where the peak returns to its original location.

While nuclear SANS data are well described by a correlated core−shell model detailing coherent structural ordering among the NPs, changes to the magnetic scattering near coercivity for both parallel and perpendicular spin orientations suggest the additional presence of uncorrelated magnetic contributions for certain field strengths. Correlated contributions (i.e., in the flakes) account for ordering in which spin alignment is consistent across multiple particles, giving rise to a diffraction peak. Reduced correlation (i.e., as described by the raspberries in the model) refers to scattering resulting from particles that are still magnetically ordered but with coherence among only a few particles, whereas uncorrelated (i.e., as described by

https://doi.org/10.1021/acsanm.3c00510
ACS Appl. Nano Mater. 2023, 6, 10986−11000

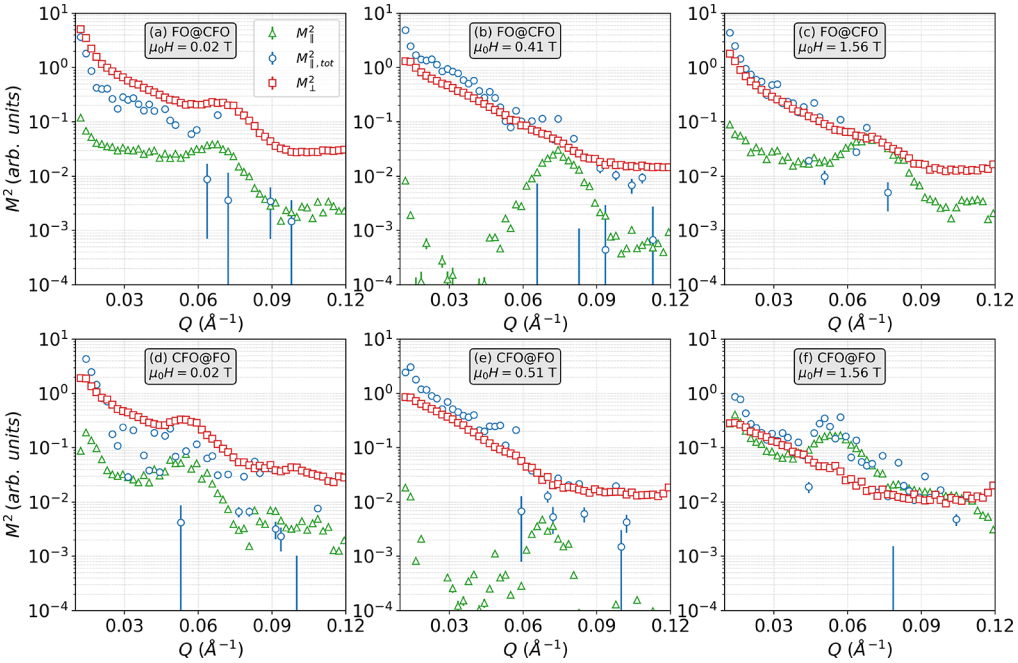

Figure 8. Perpendicular ($M^2_{\perp}$, red squares), net parallel ($M^2_{\parallel}$, green triangles), and total parallel ($M^2_{\parallel,tot}$, blue circles) magnetic scattering at 100 K and at the fields presented. Top row (a–c) presents the magnetic scattering cross sections for the FO@CFO NPs, and bottom row (d–f) presents the same for the CFO@FO variant.

independent particles in the raspberry) corresponds to no magnetic coherence between particles.[59]

The corresponding magnetic scattering data and fits are shown in Figure 7 for each CFO/FO NP variant. At 1.56 T when both samples are near saturation, the net parallel magnetic scattering is comprised only of extended interactions (from the flakes with 7 stacked layers) for FO@CFO NPs, while the inverted variant also shows a 20% contribution from shorter range correlations (from the raspberries with clusters of 13 NPs). Note, however that the parallel magnetizations of both the FO core and CFO shell are smaller than those in the CFO@FO NPs (Table 3), indicating that the FO@CFO NPs are not fully saturated in a 1.56 T field. Following application of a large, negative (−1.56 T) field, the component of the magnetization in the core and shell parallel to the applied field is still reasonably large near remanence (0.02 T) for both variants. Shorter-range correlations are of increasing importance but primarily for the CFO@FO sample (35% scattering from raspberry clusters). Though $M^2_{\parallel}$ scattering for the FO@CFO can be completely described by the flake model, it was necessary to decrease the number of hexagonal sheets from 7 to 1 in order to fit the low Q scattering, which suggests a loss of coherence in 1D from one NP crystallite plane to the next. As the field was further increased through the coercive field, the extended ordering (i.e., from flake formations) is mostly restored for both NP types, with a small addition from single, isolated magnetic particles at 0.33 T and at 0.41 T for FO@CFO and CFO@FO NPs, respectively. In the case of the CFO@FO NPs, however, the fit for 0.51 T clearly deviates from experimental results. In interpreting the results of the modeling of the $M^2_{\parallel}$ scattering (Figure 7b,d), we stress that near the coercive field (μ_0H = 0.41 and 0.51 T for CFO@FO and μ_0H = 0.33 and 0.41 T for FO@CFO), the scattering from the $M^2_{\parallel}$ cross section is orders of magnitude weaker than near the saturation field (μ_0H = 1.56 T).

The model does not fully capture the magnetic reversal behavior of the CFO@FO NPs, possibly due to complex domain formation induced by the strong CFO anisotropy. The field dependence of the relative alignment of the parallel magnetization of the core and shell, however, differs completely for the CFO@FO and FO@CFO systems. In particular, the core and shell magnetizations remain aligned with each other in the CFO@FO NPs in the measured fields of 0.02, 0.41, 0.51, and 1.56 T. While both reverse sign between 0.02 and 0.41 T, the drop in the magnitude of the net FO shell magnetization is more substantial (Table 3). In contrast in the FO@CFO system, the net magnetizations in the two regions are antialigned with each other through the coercive region (0.33 T, 0.41 T and 0.51 T) with the FO core seeming to reverse first (though gradually). The signature of this antiparallel alignment is the shifted position of the diffraction peak to higher Q. This behavior is most pronounced in 0.33 T as shown in Figure 7-d.

In addition to the net parallel magnetization, a sizable component of the magnetization is oriented perpendicular to the applied field for both NP systems, even in fields as large as 1.56 T (Table 3). In contrast to the $M^2_{\parallel}$ scattering, however, the diffraction peak in the $M^2_{\perp}$ scattering is broad at all fields (Figure 7a,c), indicating that the interparticle correlations are of much shorter range. Near the coercive field (0.33 T, 0.41 T and 0.51 T) and 1.56 T, the dominant component in the fits (60–95%) is from the raspberry model (rather than the hexagonal flake model) with cluster sizes of 9 and 7 from the FO@CFO and CFO@FO, respectively. It is notable that more than half of the raspberry scattering in these cases can be attributed to single, isolated magnetic particles. The core and shell magnetizations are aligned and are nearly matched in magnitude, though the Fe_3O_4 shell has a slightly higher magnetization in the CFO@FO system. These magnetizations systematically decrease with increasing field but persist to 1.56 T as noted previously. The exceptional case to these trends is

https://doi.org/10.1021/acsanm.3c00510
ACS Appl. Nano Mater. 2023, 6, 10986–11000

that of 0.02 T after application of a −1.56 T field, in which the diffraction peak in the perpendicular scattering (Figure 7a,c) is well-defined for both NP systems. Specifically, the longer-range perpendicular order is reflected in the fits which show a 33% and 62% contribution from the raspberry clusters for the FO@CFO and CFO@FO NPs, respectively, with the remainder from flakes and with minimal additional scattering from isolated magnetic particles. The magnitude of magnetic scattering length density (mSLD) for the perpendicular scattering at 0.02 T is significantly larger than that obtained from the fits at other fields (Table 3), suggesting that a large fraction of the magnetization is ordered perpendicular to the field in large, correlated, multiparticle domains prior to field-induced magnetization reversal.

The NP magnetization clearly has perpendicular and net parallel components at all fields considered (Table 3). It is not clear, however, if the NP moments are coherent and uniformly tilted relative to the field over a given length scale, or if the moments within each individual NP are canted in different random directions but with a small net preference for a particular orientation. To resolve this discrepancy, we consider the total scattering along the field direction as extracted using eq 6 in the Methods section, denoted as $M^2_{\parallel,tot}$. Note that the difference between the $M^2_{\parallel,tot}$ data and the $M^2_{\parallel}$ data shown in Figure 7b,d (and repeated in Figure 8) is that the former is sensitive to all moments oriented parallel or antiparallel to the field, whereas the latter is sensitive to the net magnetization parallel to the field (which corresponds to what is measured with magnetometry as in Figure 3). Strictly speaking, the $M^2_{\parallel,tot}$ scattering includes the contribution from $M^2_{\parallel}$, but the data are not particularly sensitive to the relative orientation of the core and shell magnetizations in the fits.

The $M^2_{\parallel,tot}$ scattering relative to the $M^2_{\perp}$ and $M^2_{\parallel}$ scattering at different fields at 100 K is plotted in Figure 8 for both the FO@CFO and CFO@FO NP variants. As shown in Figure 8b,e, $M^2_{\parallel,tot}$ is only slightly higher than $M^2_{\perp}$ at fields through the coercive region as the moments gradually align parallel to the field. This correspondence suggests that the magnetization of each magnetic region primarily has a random orientation in the X, Y and Z directions with a coherence that is confined mostly to single particles. In contrast, the $M^2_{\parallel,tot}$ scattering (Figures 8a,d) is somewhat lower than the $M^2_{\perp}$ scattering at 0.02 T, a field which just precedes the reversal of the net magnetization. In this case, the CFO anisotropy appears to dominate other interactions and coherently drives a large fraction of the spins perpendicular to the field, whereas a portion of the magnetization along the field direction apparently breaks into small domains (i.e., presumably smaller than the NP diameter) that are not easily detectable with our SANS configuration. A final note is that $M^2_{\parallel,tot}$ is a closer match to $M^2_{\parallel}$, rather than $M^2_{\perp}$, for the CFO@FO NPs in 1.56 T (Figure 8f), indicating that preferential orientation of the magnetization parallel to the field supplants the random orientation as the field is increased. The $M^2_{\parallel,tot}$ scattering in 1.56 T for the FO@CFO NPs (Figure 8c), however, nearly matches the $M^2_{\perp}$ scattering, indicating that a large fraction of the moments remain randomly oriented, and not saturated, in this high field.

DISCUSSION AND CONCLUSIONS

TEM micrographs of each $CoFe_2O_4/Fe_3O_4$ NP variant, shown in Figure 2, reveal nearly spherical NPs on the order of 10 nm in diameter. In the nuclear SANS scattering data presented in Figure 6, we show that the local structure of the NPs is well described with a spherical core + multishell model. The particle-to-particle distributions can be modeled with a hierarchical arrangement of the NPs, consistent with the morphology and self-assembly evident in the TEM micrographs. Also, the TEM images reveal the good epitaxy between the spinel core (either $CoFe_2O_4$ or Fe_3O_4) and the spinel ferrite shell. Magnetometry of CFO@FO NPs (Figure 3a,b) indicates a blocking temperature well above room temperature while hysteresis loops at 5 and 100 K reveal the coercive field is increasing at lower temperatures. FO@CFO NPs, shown in Figure 3c,d, have a lower blocking temperature around 275 K and smaller coercive fields values compared to the CFO@FO variants. The well-known first-order Verwey transition in Fe_3O_4, characterized by a sharp decrease in the magnetization at T_{Verwey} at 120 K, is not observed in our FO@CFO NPs as the small core size of the Fe_3O_4core (∼7 nm) and the relatively thick, high-anisotropy $CoFe_2O_4$ shell act to suppress the magneto-structural Verwey transition. A similar lack of a Verwey-type magnetization decrease is observed in Fe_3O_4 NPs with diameters similar to the core size of our FO@CFO NPs.[60]

The Langevin analysis and the modified Langevin approach, which includes additional degrees of freedom to simulate a distribution of NP moments, clearly indicate that at low fields the NPs exhibit a loss of spin alignment parallel to the applied field direction, suggesting that even at room temperature the spin reversal process for the NPs may involve a more complicated pathway than a coherent rotation of the total moment. The magnetometry also indicates a slower approach to saturation for the FO@CFO NPs than the CFO@FO variant, which is in line with the SANS analyses summarized in Table 3 where the $M^2_{\parallel}$ mSLDs for FO@CFO are suppressed relative to both the CFO@FO NPs and bulk values for Fe_3O_4 and $CoFe_2O_4$. In comparison to the standard Langevin model, the log-normal size distribution implemented in the modified Langevin approach more accurately reproduces the low-field alignment of the NP moments; however, the size estimates from the modified Langevin analysis (∼7 nm diameter, or 135 nm^3) are considerably smaller than the ensemble average sizes estimated from the structural neutron scattering cross sections (∼9.2−9.6 nm, or ∼300−350 nm^3), suggesting that additional parameters beyond a distribution of NP sizes affect the magnetization reversal process.

The mesoscale magnetics model begins to address the nature of the partially incoherent rotation of the NP magnetization. In both the CFO@FO and FO@CFO variants, the Fe_3O_4 portion of the NP is clearly the magnetically softer material with lower anisotropy. This volume of the softer phase is the most probable nucleation region for the reversal process to start. Notably, according to this model the nucleation develops at the surface of the CFO@FO NPs but in the core for the FO@CFO variation. The SANS results, in fact, clearly confirm the model's conclusion that the nucleation for reversal in FO@CFO NPs is in the Fe_3O_4 core. The mesoscale model further suggests that the interface between the two constituent materials is a pinning site that gives rise to the large coercivity in both NP systems.

In analyzing the SANS data, the nuclear (structural) scattering starts with a model that assumes a single NP structure of a core + shell or multishell with essentially smooth interfaces between the core and inner shell, as expected from the TEM imaging. However, modeling of both the structural and magnetic scattering distributions requires additional ordering among the NPs with different length scales. The

https://doi.org/10.1021/acsanm.3c00510
ACS Appl. Nano Mater. 2023, 6, 10986−11000

NP ensembles assemble into plate-like substructures with close-packed arrangements of NPs; these substructures give rise to extended correlations apparent in both the nuclear and magnetic scattering distributions. In addition, a fraction of the NPs arrange themselves into localized raspberry-type structures with reduced correlations. This model reveals that local interactions are particularly prominent near the coercive field in the perpendicular component of the magnetization.

The SANS results indicate that magnetically, both the $CoFe_2O_4$ and Fe_3O_4 phases are strongly coupled in both NP variants. Here, the common spinel structure promotes the epitaxial growth of the shell on the crystalline core and likely facilitates the magnetic coupling between core and shell. In the case of the FO@CFO system, however, the reduced SLD of the outer ∼0.5 nm of the $CoFe_2O_4$ layer may indicate some loss of structural integrity of the higher anisotropy shell material toward the outer surface of the NP. On the other hand, the lattice parameter of $CoFe_2O_4$ is ∼0.84 nm. Hence, a comparison of model fits indicates that the variation is approximately 0.5 nm, corresponding to about one-half of a unit cell. Note that SANS sensitivity to the precise thickness of this surface layer is somewhat limited at low Q as it is manifest primarily as a damping of the interference oscillations from thicker layers. A structural variation on the order of half a unit cell of the $CoFe_2O_4$ would average out to a lower SLD. The SANS analyses indicate that the cores of the FO@CFO and CFO@FO NPs are compositionally robust, while the reduced SLD values for the $CoFe_2O_4$ and Fe_3O_4 shells are suggestive of porosity, interlayer intermixing and/or off-stoichiometry in these outer layers. Unfortunately, the SANS models are not sensitive to parameters such as interfacial width and roughness due to the limited polydispersity of the NP sizes.

The field-dependent mSLD's in Table 3 indicate that after saturation at −1.56 T, which produces a negative mSLD in both the core and shell just above zero-field, in the FO@CFO NPs there is a range of positive field values (0.33 T → 0.51 T) where the magnetization directions between the core and shell are antiparallel, followed by reversal of the $CoFe_2O_4$ and parallel alignment of the core and shell magnetizations at high field. The lower anisotropy Fe_3O_4 core is the likely initial point of the magnetization reversal.

When the high anisotropy $CoFe_2O_4$ forms the core of the NP, the SANS analyses indicate that the reversal is more uniform, and the $CoFe_2O_4$ core and Fe_3O_4 shell reverse direction effectively in unison as the field is increased. However, the field hysteresis (Figure 3a) shows a step-like feature at ∼0.2 T, suggesting that there is at least a two-stage reversal. The SANS analyses for parallel alignment rely primarily on $M_{\parallel}^2$, which is quite weak near coercivity (Figure 7b). The reversal process may also be complicated by the development of magnetic domains near the coercive field, which gives rise to weak, complex scattering that cannot be described accurately within the context of our core/multishell SANS model (Figure 7b).

The SANS results also clearly point to a considerable perpendicular component ($M_{\perp}^2$) of the magnetization for both NP variants and across all field conditions. In Table 3, the effect is evident near +0.02 T after saturation at −1.56 T, and the magnitude of the $M_{\perp}^2$ component decreases monotonically as the field is increased up toward +1.56 T. The $M_{\perp}^2$ diffraction peaks in Figure 7a for CFO@FO and Figure 7c for FO@CFO are most prominent at low fields and broaden and decrease in intensity as the applied field is increased. The broader diffraction peaks in $M_{\perp}^2$, compared to similar features in $M_{\parallel}^2$, indicate a reduced coherence in the perpendicular magnetic ordering. The reduced perpendicular magnetic order may arise from a random distribution of the $CoFe_2O_4$ anisotropy axes in the NPs.

The knee-like features seen in the hysteresis loops of Figure 3 have been reported in other hard/soft systems for both NPs due to exchange spring coupling across the hard/soft interface.[7,61−63] Exchange spring coupling is strongly tied to the dimensions of the soft phase; when the size of the soft region is less than twice the length of the domain wall of the hard phase ($2\delta_H$), the system will see strong exchange coupling and a smooth hysteresis curve.[5,6,64] If the soft region is larger than this critical size, the core and shell materials will be coupled only at the interface allowing the soft layer to nucleate spin reversal at a lower field than the hard phase.[61] In core−shell NPs with overall dimensions below that of $2\delta_H$, magnetic properties are still tied to the volume of the soft phase; structures where the volume fraction of the soft material dominate have also been shown to exhibit two-phase hysteresis loops similar to those seen in Figure 3.[62,63,65−68] In the CFO@FO NPs, the softer magnetite shell comprised nearly 75% of the overall NP volume, and the magnetic effects are well explained by exchange spring coupling that pins spins near the core−shell interface while allowing spins near the surface to rotate freely as the external field is increased. In a strongly coupled system the spins in the core and shell regions behave coherently and so the spin state switching process will happen uniformly throughout the NP. Weaker coupling between core−shell layers can lead to pinned shell spins near the interface while those closer to the surface are free to rotate independently of core and interface spins.

The spin evolution with field is more complex in the inverted FO@CFO system. In these NPs, the softer Fe_3O_4 phase occupies only ∼39% of the total volume, down from ∼75% in the hard@soft CFO@FO variant. However, the core size is larger in the FO@CFO NPs. From Figure 3c, the knee-like features common in hysteresis loops of exchange-spring magnets are present at 5 K but noticeably absent at 100 K, and, despite a greater hard phase volume fraction, the coercivities are lower than those seen for the CFO@FO NPs. In the conventional hard@soft variant the $CoFe_2O_4$ layer only has one interface for coupling to occur whereas in the inverted system when CFO is located in the shell, interfacial effects can happen at the core−shell boundary and at the surface. As the Zeeman energy increases, spins in the FO core can easily switch direction while those in the CFO shell face competing spin disordering effects at both the core−shell interface and at the surface. The SANS analyses also suggest that the $CoFe_2O_4$ structural integrity may be degraded somewhat toward the surface of the NP, which may reduce the magnetocrystalline anisotropy of the CFO as reflected in the lower coercive field of the FO@CFO NPs. Also, a larger Fe_3O_4 core also means more $CoFe_2O_4$ spins will be located at the core−shell interface due to the increased surface area which, in combination with disordering at two interfaces, could result in a smaller measured coercive field.

In summary, we have examined spin ordering in all-spinel ferrite, quasi-spherical core−shell NPs which pair high-anisotropy $CoFe_2O_4$ with magnetically softer and higher moment Fe_3O_4. The magnetic properties of the NPs are greatly modified by varying the selection of ferrite in the core and shell, and we examine the local and longer-range spin

https://doi.org/10.1021/acsanm.3c00510
ACS Appl. Nano Mater. 2023, 6, 10986−11000

ordering in the NPs with magnetometry, mesoscale magnetic simulations, and fully polarized SANS. A mean-field (Langevin) model of room-temperature field hysteresis indicates a loss of spin order relative to isolated macrospins representing the NPs, while the mesoscale magnetic model suggests that interfacial coupling between the hard/soft layers leads to a noncollinear arrangement of spins in the core and shell.

Small angle neutron scattering reveals both extended interactions with close-packed flake-like structures as well as the presence of shorter length-scale, more disordered structures, represented as the "raspberries" in our model. Magnetically, the SANS reveals a complex field reversal mechanism. Application of a small positive field after saturation in the opposite direction results in a considerable spin alignment in both the parallel and perpendicular directions that is coherent across the close-packed, local structure. As the system is driven toward and through the coercive field, the net parallel scattering weakens considerably, and the coherent peak shifts to higher Q for the FO@CFO system. Modeling indicates that in the FO@CFO system, the approach toward coercivity results in an anti-alignment of the core and shell magnetizations, strongly suggesting that the softer Fe_3O_4 core is the nucleation site for the reversal of the magnetization which is in line with the mesoscale magnetic simulations. For the CFO@FO variant, the reversal of the magnetization is more uniform throughout the NP. However, in both systems at high fields the core and shell magnetizations are mostly aligned with the field, as expected. Somewhat surprisingly, even at near-saturation, the system retains a high degree of perpendicular magnetic scattering.

Our results indicate that in addition to properties such as material selection (which establishes the bulk magnetization and anisotropy of the constituents) and overall NP size, additional parameters including core−shell volume ratios and number of interfaces of the magnetically hard component (core to shell vs shell to core + shell to surfactant layer) greatly affect the overall spin ordering within NPs and across ensembles of NPs. Control over these parameters will facilitate development of versatile magnetic NPs with properties optimized for disparate applications ranging from biomedicine, environmental remediation, information storage and other fields.

METHODS

Sample Synthesis, Magnetometry, and Nanoparticle Imaging. Two variants of $CoFe_2O_4$ and Fe_3O_4 NPs were studied: Using the notation of core@shell to represent the materials in each layer of the NP, one variant was composed of $CoFe_2O_4$ in the core and Fe_3O_4 in the shell layer (CFO@FO), while the inverted structure (FO@CFO) was the second NP studied. Both structures were synthesized via a similar seed mediated thermal decomposition process using 1,2 hexadecanediol, oleic acid (90%), oleylamine (70%), and benzyl ether (98%) with iron(III) acetylacetonate to make Fe_3O_4 while adding cobalt(II) acetylacetonate to the mix would produce $CoFe_2O_4$ instead. For FO cores, the temperature of mixture was raised to 200 °C, kept there for 2 h in a nitrogen gas environment before increasing temperature to 300 °C and refluxing for 1 h. For the CFO cores, after the initial heating at 200 °C for 2 h, the temperature was slowly increased at a ramping rate of 3 °C/min to 300 °C and refluxed for 30 min. The mixture was then cooled to room temperature after which the cores were washed and collected by centrifuging with ethanol and hexane.

The cores were then dispersed in hexane to be used as seeds for the shell layer growth; 85 mg of synthesized core were added to the above mixtures for Fe_3O_4 or $CoFe_2O_4$, depending on the desired shell composition. The core-mixture was then heated to 100 °C for 30 min to evaporate the hexane before refluxing at 300 °C for 1 h. The now synthesized core−shell NPs were cooled to room temperature before being washed in ethanol and collected by centrifuging the mixture. The NPs were mixed with a small amount of hexane to prevent further oxidation or side reactions from occurring. This synthesis is known to produce NPs with a core 6 nm in diameter surrounded by a roughly 1−2 nm thick shell. Details on synthesis methods have been published elsewhere.[69−71]

A high-field superconducting magnet + cryostat system equipped with a vibrating sample magnetometer was used to measure the average magnetization of the synthesized powder. The closed cycle cryostat spans a temperature range of 1.8−400 K and the magnet can provide magnetic fields up to ±9 T. High-resolution transmission electron microscopy (TEM) images were acquired in bright field mode. The powder sample was diluted in a small amount of hexane and ultrasonicated to prevent agglomeration of the NPs. One drop of the well-dispersed NP solution was then placed on a copper TEM grid and dried in air to evaporate the hexane before insertion into the imaging column.

Mesoscale Magnetic Modeling. A simplified Hamiltonian is used for each NP that separates the core and shell into distinct macrospins and contains terms for the core−shell exchange and possible direct exchange between different NPs (in the case of close contact between particles):

$$\mathcal{H} = -\sum_{i,j} J_{ij} S_i S_j - \sum_i k(\cos)^2 \varphi_i - g\mu_B \sum_i S_i B + \sum_{m,n} M_m [D] M_n - \sum_{m,n} J_{inter} M_m M_n \quad (2)$$

In this expression, $\{S_i\}$ represents the moment of macro spins within a NP, while $\{M_n\}$ is the net moment of particle n, so that indices $\{i, j\}$ denote summation within a NP while $\{m, n\}$ denote interactions between NPs. J_{ij} is the Heisenberg interaction coupling between macrospins i and j within a single NP. The magnetic anisotropy constant is represented by k and ϕ_i is the angle between S_i and easy axis direction, while $\boldsymbol{B}$ is the external magnetic field. The fourth term represents dipolar interactions between the net moment of each NP with moment M_n while $[\boldsymbol{D}]$ is the dipolar tensor. The same notation holds for the last term of the Hamiltonian which describes interparticle interactions of the Heisenberg form with strength J_{inter}. Temperature effects are simulated with the usual Boltzmann approach, and Monte Carlo methods are used to ensure sufficient sampling of the configuration space.

For each NP, the total magnetic moment is subdivided into six macrospins, three each for the core and shell, and the sum of the macrospins for the core and shell equals the total moment per NP, as determined from bulk magnetometry. The volume ratio of the core and the shell can be determined from the structural (spin averaged) neutron scattering, as described below, and this ratio can be used to estimate the total moment per NP separately for the core and the shell. For the CFO@FO variant, the core−shell moments are estimated as 4.14×10^{-20} Am^2/12.38×10^{-20} Am^2 [FO@CFO: 6.80×10^{-20} Am^2/10.74×10^{-20} Am^2]. The multiple macrospins per core and shell can simulate the effects of spin variations at the core−shell and shell/vacuum interface. The ensemble of NPs is simulated by placing the macrospins for each NP on a $12 \times 12 \times 12$ grid (i.e., 12^3 NPs) with a mean spacing of 10 nm between NPs and then imposing periodic boundary conditions.

SANS Instrumentation and Data Reduction. Polarized SANS measurements were completed at the NIST Center for Neutron Research using NG-7, a 30 m small angle neutron scattering instrument.[72] A fully polarized configuration was employed that uses an FeSi supermirror in front of the sample holder to initially polarize neutrons in a spin up orientation with a RF flipper coil that can reverse the spin direction of the incident neutron beam. A ^{3}He cell located after the sample environment moderates the final neutron spin state by only allowing spins aligned with the ^{3}He nuclear spins to

https://doi.org/10.1021/acsanm.3c00510
ACS Appl. Nano Mater. 2023, 6, 10986−11000

pass; the direction of the ^{3}He spins is reversed with a nuclear magnetic resonance pulse.[73] In between both pieces of polarizing equipment is the sample environment where both $CoFe_2O_4/Fe_3O_4$ NPs were mounted in a closed cycle refrigerator in an aluminum holder backfilled with He to prevent degradation of the samples during measurements. An electromagnet capable of horizontal fields up to ∼1.56 T was used for all measurements. On NG-7, the neutron beam is oriented in the Z direction and scattering in the XY plane is collected with a 2D detector (refer to Figure 4 for coordinate system). The detector position relative to the sample was fixed at either 8 m or 2 m to cover a broad range of scattering vectors (Q). The 2D scattering profiles were reduced using a custom Python script[74] and analyzed in SASView 4.2.2[75] using a custom core/multishell model.

SANS measurements produce 2D scattering distributions where the intensity is related to the squared sum of the nuclear and magnetic Fourier transforms.[76] In a fully polarized SANS setup the neutron direction is established before and after interacting with the sample allowing for measurements of all four scattering cross sections; spin up (↑) indicates a neutron that is aligned parallel to an external field while a spin down (↓) neutron is antiparallel to the field. When a neutron maintains the same orientation before and after scattering from the sample, it is known as a non spin-flip (NSF) interaction (↑↑ or ↓↓), whereas a spin-flip (SF) interaction measures cross sections where the neutron spin changes direction (↑↓ or ↓↑).

The 2D detector captures scattering in the $X-Y$ plane orthogonal to the neutron beam, and sector cuts at key angles with widths of ±10° are averaged from these profiles. These sector cuts allow for calculation of individual nuclear (N^2) and perpendicular or parallel magnetic ($M_\perp^2$ and $M_\parallel^2$, respectively) scattering contributions, where θ is the angle between the applied field in the X-direction and the scattering vector Q in the $X-Y$ plane (inset Figure 5b). The angular dependence of both nuclear and magnetic scattering along with the neutron spin selection rules, in which the scattering is sensitive only to the magnetization perpendicular to Q, allows for a simplified analysis of individual scattering contributions at key angles.[77] Specifically, at $\theta = 0°$ and at $\theta = 90°$ the SF scattering is sensitive only to the projection of the magnetization that is perpendicular to the applied field. The NSF scattering is related to the structure and to the component of the magnetization parallel to the field at $\theta = 90°$, but detects only the structure at $\theta = 0°$. These angle-dependent polarization rules simplify as follows:

$$N^2(Q) = (I^{\uparrow\uparrow}_{\theta=0°} + I^{\downarrow\downarrow}_{\theta=0°}) \tag{3}$$

$$M_\parallel^2(Q) = \frac{(I^{\downarrow\downarrow}_{\theta=90°} - I^{\uparrow\uparrow}_{\theta=90°})^2}{4N^2} \tag{4}$$

$$M_\perp^2(Q) = \frac{1}{3}[(I^{\uparrow\downarrow}_{\theta=0°} + I^{\downarrow\uparrow}_{\theta=0°}) + (I^{\uparrow\downarrow}_{\theta=90°} + I^{\downarrow\uparrow}_{\theta=90°})] \tag{5}$$

$$M_{\parallel,tot}^2(Q) = (I^{\uparrow\uparrow}_{\theta=90°} + I^{\downarrow\downarrow}_{\theta=90°}) - (I^{\uparrow\uparrow}_{\theta=0°} + I^{\downarrow\downarrow}_{\theta=0°}) \tag{6}$$

where (↑, ↓) indicate scattering from spin up and down neutrons, respectively, and I^{pq} corresponds to the scattering intensity along that sector cut angle for the initial spin direction, p, and the selected spin direction after scattering, q.[16,73,78] Note that it is assumed that the $I^{\uparrow\uparrow}$, $I^{\downarrow\downarrow}$, $I^{\uparrow\downarrow}$, and $I^{\downarrow\uparrow}$ scattered intensities are normalized by the unpolarized main beam intensity. Each equation assumes isotropic nuclear scattering (N^2), $M_\parallel^2 = M_X^2$, and isotropic magnetic scattering orthogonal to the applied field $M_\perp^2 = M_Y^2 = M_Z^2$.[77] Note that the first parenthetical term on the right of eq 5 is equal to $M_Z^2 + M_Y^2$ and the second parenthetical term is equal to M_Z^2. Eq 4 is sensitive to the net magnetization parallel to the applied field, and $M_\parallel^2$ will decrease at lower fields when spins are less aligned; the smaller magnitude of $M_\parallel^2$ near the coercive field results in lower signal-to-noise ratios. As a complement, $M_{\parallel,tot}^2$ (eq 6) corresponds to the square of the total magnetization along the X axis that is parallel and/or antiparallel to the applied field. When the magnetization is randomly oriented near the coercive field, it is expected that $M_{\parallel,tot}^2 = M_\perp^2$ even though the net magnetization along the field direction will be small.

SANS Modeling. To account for the NP close packing and clustering as well as for the internal NP core/multishell structure, a complex model was used to fit the structural and magnetic SANS data. The model parameterizes the NPs as spherical core−shell or core−shell 1/shell 2 structures with a Gaussian distribution of core sizes and smooth core−shell interfaces. Consistent with the local and finite close-packed structures observed in TEM images, these dried NPs are then assumed to predominantly self-assemble into hexagonal flakes (refer to schematic in Figure 6c and ref 26). In the model, these two-dimensional "flakes" or plates are comprised of close-packed NPs with fixed separation, analogous to the Paracrystal model in the SasView fitting software (ref 79). The primary difference is that each plate in the flake model is assumed to consist of 14 or 16 (for FO@CFO and CFO@FO, respectively) NPs arranged in a hexagon with 6 stacked layers that are offset to approximate the local face-centered-cubic packing. The calculated scattering is then averaged over all random orientation of the flakes in space. The calculations from the flake model accurately reproduce the structural diffraction peaks at $Q \simeq 0.055$ and 0.07 Å for the CFO@FO and FO@CFO NPs, respectively (Figures 6a,b), but there are issues at lower Q. For the FO@CFO sample, the slight oscillations in the fit are assumed to be insignificant as they likely originate from the discrete increments in angular position used to generate the random orientations of the flakes in the model. For the CFO@FO structural case, the flake model consistently undershoots the low Q scattering.

The underestimate of the "flake" model at low momentum transfer in the case of the CFO@FO NPs was resolved with the addition of a contribution for core/multishell NP clusters arranged in a "raspberry" configuration (ref 80) to account for the presence of self-assembled NP clusters (refer to schematic in Figure 6c). For the CFO@FO system, these "raspberries" consisted of 12 identical core−shell NPs packed around on the surface of a single, central NP. These small structures give rise to a broad scattering feature for Q values below the diffraction peak. The fit in Figure 6b demonstrates that the structural scattering is well described over all Q by a model with additive contributions from both the flake and raspberry models. In contrast, no raspberry contribution was included in the model for the FO@CFO case (Figure 6a). It is important to note that this core−shell model with both raspberry and flake contributions is not unique due to the phase problem that is intrinsic to elastic scattering data. This model, however, is firmly based upon known physical characteristics of the system (i.e., local self-assembly) and is not over determined. As demonstrated in this manuscript, it best provides a self-consistent description of the structural and magnetic SANS data (eqs 3−5) for both samples over a range of applied fields. Modeling of CFO@FO core−shell NPs was completed over an extended Q-range in order to accurately describe the scattering over a range of length scales, though Figure 6 focuses only on the region near the diffraction peak.

All magnetic SANS data were analyzed with the same model as used for the structure which includes raspberry and flake-like clusters of spherical core + multishell particles. To include magnetic contributions from correlations at various length scales that differ from the structural correlations, the number of NPs comprising the raspberry was varied with field, and a percentage of these NPs (as described by the "surface fraction" fitting parameter)[80] were assumed to independently contribute to the magnetic scattering. In addition, it was assumed that the magnetic moments in each two-dimensional flake were not subject to magnetic shape anisotropy. Specifically, the parallel and perpendicular magnetic components (eqs 4 and 5) are assumed to be equivalent along every direction within the randomly oriented flakes.

While both the parallel and perpendicular magnetic scattering for the CFO@FO could be described with particles with a core and single FO shell, it was necessary to divide the shell of the FO@CFO sample into two sections to self-consistently fit the structural, perpendicular magnetic, and parallel magnetic scattering with a single model. As described previously, we speculate that the presence of an outermost shell with a reduced structural SLD indicates that the CFO on the surface is porous, rough, or chemically different. The fits to the magnetic structure, shown in Figure 7, reveal that the magnetization

https://doi.org/10.1021/acsanm.3c00510
ACS Appl. Nano Mater. 2023, 6, 10986−11000

of this outer layer aligns with that of the inner CFO shell although the magnitude of the magnetic SLD is consistently lower in this outer layer.

AUTHOR INFORMATION

Corresponding Author

Darío A. Arena − *Department of Physics, University of South Florida, Tampa, Florida 33620, United States;* orcid.org/0000-0001-7463-6472; Email: darena@usf.edu

Authors

Corisa Kons − *Department of Physics, University of South Florida, Tampa, Florida 33620, United States*

Kathryn L. Krycka − *National Institute of Standards and Technology, Gaithersburg, Maryland 20899, United States*

Joshua Robles − *Department of Physics, University of South Florida, Tampa, Florida 33620, United States*

Nikolaos Ntallis − *Department of Physics and Astronomy, Uppsala University, Uppsala 751 05, Sweden*

Manuel Pereiro − *Department of Physics and Astronomy, Uppsala University, Uppsala 751 05, Sweden;* orcid.org/0000-0003-2977-255X

Manh-Huong Phan − *Department of Physics, University of South Florida, Tampa, Florida 33620, United States;* orcid.org/0000-0002-6270-8990

Hariharan Srikanth − *Department of Physics, University of South Florida, Tampa, Florida 33620, United States;* orcid.org/0000-0002-2541-7000

Julie A. Borchers − *National Institute of Standards and Technology, Gaithersburg, Maryland 20899, United States*

Complete contact information is available at: https://pubs.acs.org/10.1021/acsanm.3c00510

Notes

The authors declare no competing financial interest.

ACKNOWLEDGMENTS

The authors would like to thank Dr. Javier Alonso Masa, Department of Earth Sciences and Condensed Matter Physics at the University of Cantabria, Spain for his help with the modified Langevin model. We are grateful to Jeff Krzywon for technical assistance on NG7 and to Shannon Watson and Taufique Hassan for assistance with the ^{3}He polarization analyzer. This material is based upon work supported by the National Science Foundation under grant no. ECCS-1952957. D.A.A. acknowledges the support of the USF Nexus Initiative and the Swedish Fulbright Commission. H.S. and M.H.P. acknowledge support from US Department of Energy, Office of Basic Energy Sciences, Division of Materials Science and Engineering under award no. DE-FG02-07ER46438. H.S. also thanks the Alexander von Humboldt foundation for a research award. N.N. and M.P. acknowledge financial support from Knut and Alice Wallenberg Foundation through grant no. 2018.0060. Some of the computations were performed on resources provided by the Swedish National Infrastructure for Computing (SNIC) at the National Supercomputer Center (NSC), Linköping University, the PDC Centre for High Performance Computing (PDC-HPC), KTH, and the High Performance Computing Center North (HPC2N), Umeå University. Access to polarization capabilities on the NG7 SANS instrument was provided by the Center for High Resolution Neutron Scattering, a partnership between the National Institute of Standards and Technology and the National Science Foundation under agreement no. DMR-2010792.

REFERENCES

(1) Reier, T.; Oezaslan, M.; Strasser, P. Electrocatalytic oxygen evolution reaction (OER) on Ru, Ir, and Pt catalysts: A comparative study of nanoparticles and bulk materials. *ACS Catal.* **2012**, *2*, 1765−1772.

(2) Caizer, C. In *Handbook of Nanoparticles*; Aliofkhazraei, M., Ed.; Springer International Publishing: Cham, 2016; pp 475−519.

(3) Cao, L.-F.; Xie, D.; Guo, M.-X.; Park, H.; Fujita, T. Size and shape effects on Curie temperature of ferromagnetic nanoparticles. *Transactions of Nonferrous Metals Society of China* **2007**, *17*, 1451−1455.

(4) Fauth, K.; Goering, E.; Schütz, G.; Kuhn, L. T. Probing composition and interfacial interaction in oxide passivated core-shell iron nanoparticles by combining x-ray absorption and magnetic circular dichroism. *J. Appl. Phys.* **2004**, *96*, 399−403.

(5) Kneller, E. F.; Hawig, R. The exchange-spring magnet: a new material principle for permanent magnets. *IEEE Trans. Magn.* **1991**, *27*, 3588−3560.

(6) Skomski, R.; Coey, J. M. D. Exchange coupling and energy product in random two-phase aligned magnets. *IEEE Trans. Magn.* **1994**, *30*, 607−609.

(7) Liu, F.; Hou, Y.; Gao, S. Exchange-coupled nanocomposites: chemical synthesis, characterization and applications. *Chem. Soc. Rev.* **2014**, *43*, 8098−8113.

(8) Sartori, K.; Cotin, G.; Bouillet, C.; Halté, V.; Bégin-Colin, S.; Choueikani, F.; Pichon, B. P. Strong interfacial coupling through exchange interactions in soft/hard core−shell nanoparticles as a function of cationic distribution. *Nanoscale* **2019**, *11*, 12946−12958.

(9) Lavorato, G. C.; Das, R.; Xing, Y.; Robles, J.; Litterst, F. J.; Baggio-Saitovitch, E.; Phan, M.-H.; Srikanth, H. Origin and shell-driven optimization of the heating power in core−shell bimagnetic nanoparticles. *ACS Applied Nano Materials* **2020**, *3*, 1755−1765.

(10) Sanna Angotzi, M.; Mameli, V.; Cara, C.; Musinu, A.; Sangregorio, C.; Niznansky, D.; Xin, H. L.; Vejpravova, J.; Cannas, C. Coupled hard−soft spinel ferrite-based core−shell nanoarchitectures: magnetic properties and heating abilities. *Nanoscale Adv.* **2020**, *2*, 3191−3201.

(11) Kefeni, K. K.; Msagati, T. A.; Mamba, B. B. Ferrite nanoparticles: Synthesis, characterisation and applications in electronic device. *Materials Science and Engineering: B* **2017**, *215*, 37−55.

(12) Quesada, A.; et al. Energy product enhancement in imperfectly exchange-coupled nanocomposite magnets. *Advanced Electronic Materials* **2016**, *2*, 1500365.

(13) Batlle, X.; Labarta, A. Finite-size effects in fine particles: magnetic and transport properties. *Journal of Physics D* **2002**, *35*, 201.

(14) Issa, B.; Obaidat, I. M.; Albiss, B. A.; Haik, Y. Magnetic nanoparticles: surface effects and properties related to biomedicine applications. *International Journal of Molecular Sciences* **2013**, *14*, 21266−21305.

(15) Coey, J. M. D. Noncollinear spin arrangement in ultrafine ferrimagnetic crystallites. *Phys. Rev. Lett.* **1971**, *27*, 1140−1142.

(16) Krycka, K. L.; Booth, R. A.; Hogg, C. R.; Ijiri, Y.; Borchers, J. A.; Chen, W. C.; Watson, S. M.; Laver, M.; Gentile, T. R.; Dedon, L. R.; Harris, S.; Rhyne, J. J.; Majetich, S. A. Core-shell magnetic morphology of structurally uniform magnetite nanoparticles. *Phys. Rev. Lett.* **2010**, *104*, 207203.

(17) Hasz, K.; Ijiri, Y.; Krycka, K. L.; Borchers, J. A.; Booth, R. A.; Oberdick, S.; Majetich, S. A. Particle moment canting in $CoFe_2O_4$ nanoparticles. *Phys. Rev. B* **2014**, *90*, 180405.

(18) Oberdick, S.; et al. Spin canting across core−shell Fe_3O_4/$MnxFe_3$-xO_4 nanoparticles. *Sci. Rep.* **2018**, *8*, 3425.

(19) Marx, J.; Huang, H.; Salih, K.; Thiel, W.; Schünemann, V. Spin canting in ferrite nanoparticles. *Hyperfine Interact.* **2016**, *237*, 1.

(20) Peddis, D.; Mansilla, M. V.; Mørup, S.; Cannas, C.; Musinu, A.; Piccaluga, G.; D'Orazio, F.; Lucari, F.; Fiorani, D. Spin-canting and

magnetic anisotropy in ultrasmall $CoFe_2O_4$ nanoparticles. *J. Phys. Chem. B* **2008**, *112*, 8507−8513.
(21) Peddis, D.; Yaacoub, N.; Ferretti, M.; Martinelli, A.; Piccaluga, G.; Musinu, A.; Cannas, C.; Navarra, G.; Greneche, J.; Fiorani, D. Cationic distribution and spin canting in $CoFe_2O_4$ nanoparticles. *J. Phys.: Condens. Matter* **2011**, *23*, 426004.
(22) Negi, D. S.; Sharona, H.; Bhat, U.; Palchoudhury, S.; Gupta, A.; Datta, R. Surface spin canting in Fe_3O_4 and $CoFe_2O_4$ nanoparticles probed by high-resolution electron energy loss spectroscopy. *Phys. Rev. B* **2017**, *95*, 174444.
(23) Ngo, A. T.; Bonville, P.; Pileni, M. P. Spin canting and size effects in nanoparticles of nonstoichiometric cobalt ferrite. *J. Appl. Phys.* **2001**, *89*, 3370−3376.
(24) Soler, M.; Paterno, L. In *Nanostructures*; Da Róz, A. L., Ferreira, M., de Lima Leite, F., Oliveira, O. N., Eds.; William Andrew Publishing, 2017; pp 147 − 186.
(25) Amiri, M.; Salavati-Niasari, M.; Akbari, A. Magnetic nanocarriers: Evolution of spinel ferrites for medical applications. *Adv. Colloid Interface Sci.* **2019**, *265*, 29−44.
(26) Ijiri, Y.; Krycka, K. L.; Hunt-Isaak, I.; Pan, H.; Hsieh, J.; Borchers, J. A.; Rhyne, J. J.; Oberdick, S. D.; Abdelgawad, A.; Majetich, S. A. Correlated spin canting in ordered core-shell Fe_3O_4/$MnxFe_3$-x O_4 nanoparticle assemblies. *Phys. Rev. B* **2019**, *99*, 094421.
(27) Coey, J. M. D. *Magnetism and magnetic materials.*; Cambridge University Press, 2010.
(28) Attanayake, S. B.; Chanda, A.; Das, R.; Kapuruge, N.; Gutierrez, H. R.; Phan, M. H.; Srikanth, H. Emergent magnetism and exchange bias effect in iron oxide nanocubes with tunable phase and size. *J. Phys.: Condens. Matter* **2022**, *34*, 495301.
(29) Kim, T.; Sim, S.; Lim, S.; Patino, M. A.; Hong, J.; Lee, J.; Hyeon, T.; Shimakawa, Y.; Lee, S.; Attfield, J. P.; Park, J. G. Slow oxidation of magnetite nanoparticles elucidates the limits of the Verwey transition. *Nat. Commun.* **2021**, *12*, 10−15.
(30) Zeng, H.; Sun, S. Syntheses, Properties, and Potential Applications of Multicomponent Magnetic Nanoparticles. *Adv. Funct. Mater.* **2008**, *18*, 391−400.
(31) Mohtasebzadeh, A. R.; Davidson, J. C.; Livesey, K. L.; Crawford, T. M. Tunability and ordering in 2D arrays of magnetic nanoparticles assembled via extreme field gradients. *Adv. Mater. Interfaces* **2022**, *9*, 2201056.
(32) Yang, Z.; Chen, Y.; Liu, W.; Wang, Y.; Li, Y.; Zhang, D.; Lu, Q.; Wu, Q.; Zhang, H.; Yue, M. Effects of shape anisotropy on hard-soft exchange-coupled permanent magnets. *Nanomatter* **2022**, *12*, 1261.
(33) Barrera, G.; Allia, P.; Tiberto, P. Magnetization dynamics of superparamagnetic nanoparticles for magnetic particle spectroscopy and imaging. *Phys. Rev. Appl.* **2022**, *18*, 024077.
(34) Dennis, C. L.; Jackson, A. J.; Borchers, J. A.; Hoopes, P. J.; Strawbridge, R.; Foreman, A. R.; Van Lierop, J.; Grüttner, C.; Ivkov, R. Nearly complete regression of tumors via collective behavior of magnetic nanoparticles in hyperthermia. *Nanotechnology* **2009**, *20*, 395103.
(35) Mosiniewicz-Szablewska, E.; Tedesco, A. C.; Suchocki, P.; Morais, P. C. Magnetic studies of polylactic-co-glicolic acid nanocapsules loaded with selol and γ-Fe_2O_3 nanoparticles. *Phys. Chem. Chem. Phys.* **2020**, *22*, 21042−21058.
(36) Lavorato, G. C.; Das, R.; Alonso Masa, J.; Phan, M. H.; Srikanth, H. Hybrid magnetic nanoparticles as efficient nanoheaters in biomedical applications. *Nanoscale Adv.* **2021**, *3*, 867−888.
(37) Hu, L.; Sun, X.; Zhou, F.; Qi, J.; Wang, A.; Wang, C.; Liu, M.; Feng, M. Magnetic coupling modulation of flexible Fe_3O_4/$CoFe_2O_4$ heterojunction grown on mica. *Ceram. Int.* **2021**, *47*, 2672−2677.
(38) Zeng, Q.; Jiang, D.; Yang, S. Enhancement of magnetic properties in hard/soft $CoFe_2O_4$/Fe_3O_4 nanocomposites. *RSC Adv.* **2016**, *6*, 46143−46148.
(39) Kuila, S.; Tiwary, S.; Sahoo, M. R.; Barik, A.; Babu, P. D.; Vishwakarma, P. N. Magnetic proximity effect in $CoFe_2O_4$ @ $BiFeO_3$ core-shell nanoparticles. *AIP Conf. Proc.* **2019**, *2115*, 030509.
(40) Golosovsky, I. V.; Salazar-Alvarez, G.; López-Ortega, A.; González, M. A.; Sort, J.; Estrader, M.; Suriñach, S.; Baró, M. D.; Nogués, J. Magnetic proximity effect features in antiferromagnetic/ferrimagnetic core-shell nanoparticles. *Phys. Rev. Lett.* **2009**, *102*, 247201.
(41) Manna, P. K.; Yusuf, S.; Basu, M.; Pal, T. The magnetic proximity effect in a ferrimagnetic Fe_3O_4 core/ferrimagnetic-Mn_2O_3 shell nanoparticle system. *J. Phys.: Condens. Matter* **2011**, *23*, 506004.
(42) Manna, P.; Yusuf, S. Two interface effects: Exchange bias and magnetic proximity. *Phys. Rep.* **2014**, *535*, 61−99.
(43) Kückelhaus, S.; Garcia, V. A.; Lacava, L. M.; Azevedo, R. B.; Lacava, Z. G.; Lima, E. C.; Figueiredo, F.; Tedesco, A. C.; Morais, P. C. Biological investigation of a citrate-coated cobalt−ferrite-based magnetic fluid. *J. Appl. Phys.* **2003**, *93*, 6707−6708.
(44) Kückelhaus, S.; Reis, S. C.; Carneiro, M. F.; Tedesco, A. C.; Oliveira, D. M.; Lima, E. C.; Morais, P. C.; Azevedo, R. B.; Lacava, Z. G. In vivo investigation of cobalt ferrite-based magnetic fluid and magnetoliposomes using morphological tests. *J. Magn. Magn. Mater.* **2004**, *272*−*276*, 2402−2403.
(45) Kückelhaus, S.; Tedesco, A. C.; Oliveira, D. M.; Morais, P. C.; Boaventura, G. R.; Lacava, Z. G. Optical emission spectroscopy as a tool for the biodistribution investigation of cobalt-ferrite nanoparticles in mice. *J. Appl. Phys.* **2005**, *97*, 10Q910.
(46) Petrarca, C.; Poma, A. M.; Vecchiotti, G.; Bernardini, G.; Niu, Q.; Cattaneo, A. G.; Di Gioacchino, M.; Sabbioni, E. Cobalt magnetic nanoparticles as theranostics: Conceivable or forgettable? *Nanotechnol. Rev.* **2020**, *9*, 1522−1538.
(47) Andrade, P. L.; Silva, V. A.; Krycka, K. L.; Leão, J. B.; Liu, I. L.; Silva, M. P.; Aguiar, J. A. The effect of organic coatings in the magnetization of $CoFe_2O_4$ nanoparticles. *AIP Adv.* **2022**, *12*, 85102.
(48) Zakutna, D.; Fischer, A.; Dresen, D.; Niznansky, D.; Honecker, D.; Disch, S. Multiscale magnetization in cobalt-doped ferrite nanocubes. *J. Appl. Crystallogr.* **2022**, *55*, 1622−1630.
(49) Honecker, D.; Bersweiler, M.; Erokhin, S.; Berkov, D.; Chesnel, K.; Venero, D. A.; Qdemat, A.; Disch, S.; Jochum, J. K.; Michels, A.; Bender, P. Using small-angle scattering to guide functional magnetic nanoparticle design. *Nanoscale Adv.* **2022**, *4*, 1026−1059.
(50) Das, B.; Batley, J. T.; Krycka, K. L.; Borchers, J. A.; Quarterman, P.; Korostynski, C.; Nguyen, M.; Kamboj, I.; Aydil, E. S.; Leighton, C. Chemically induced magnetic dead shells in superparamagnetic ni nanoparticles deduced from polarized small-angle neutron scattering. *ACS Appl. Mater. Interfaces* **2022**, *14*, 33491.
(51) Nemati, Z.; Khurshid, H.; Alonso, J.; Phan, M. H.; Mukherjee, P.; Srikanth, H. From core−shell to hollow Fe/γ-Fe_2O_3 nanoparticles: evolution of the magnetic behavior. *Nanotechnology* **2015**, *26*, 405705.
(52) Fiorani, D.; Peddis, D. Understanding dynamics of interacting magnetic nanoparticles: from the weak interaction regime to the collective superspin glass state. *Journal of Physics: Conference Series* **2014**, *521*, 012006.
(53) Silva, N. J. O.; Amaral, V. S.; Carlos, L. D. Relevance of magnetic moment distribution and scaling law methods to study the magnetic behavior of antiferromagnetic nanoparticles: Application to ferritin. *Phys. Rev. B* **2005**, *71*, 184408.
(54) Kons, C.; Srikanth, H.; Phan, M.-H.; Arena, D. A.; Pereiro, M. Macrospin model of an assembly of magnetically coupled core-shell nanoparticles. *Phys. Rev. B* **2022**, *106*, 104402.
(55) Zhu, Y., Ed. *Modern Techniques for Characterizing Magnetic Materials*; Springer US: Boston, MA, 2005; pp 107−155.
(56) Bonini, M.; Wiedenmann, A.; Baglioni, P. Study of ferrite ferrofluids by small-angle scattering of polarized neutrons. *J. Appl. Crystallogr.* **2007**, *40*, s254−s258.
(57) Nagornyi, A.; Avdeev, M.; Yelenich, O.; Solopan, S.; Belous, A.; Shulenina, A.; Turchenko, V.; Soloviov, D.; Bulavin, L.; Aksenov, V. Structural aspects of Fe_3O_4/$CoFe_2O_4$ magnetic nanoparticles according to x-ray and neutron scattering. *Journal of Surface Investigation: X-ray, Synchrotron and Neutron Techniques* **2018**, *12*, 737−743.
(58) Vivas, L. G.; Yanes, R.; Michels, A. Small-angle neutron scattering modeling of spin disorder in nanoparticles. *Sci. Rep.* **2017**, *7*, 13060.

https://doi.org/10.1021/acsanm.3c00510
ACS Appl. Nano Mater. 2023, 6, 10986−11000

(59) Honecker, D.; Fernández Barquín, L.; Bender, P. Magnetic structure factor of correlated moments in small-angle neutron scattering. *Phys. Rev. B* **2020**, *101*, 134401.
(60) Allia, P.; Barrera, G.; Tiberto, P. Fe_3O_4 nanoparticles and nanocomposites with potential application in biomedicine and in communication technologies: Nanoparticle aggregation, interaction, and effective magnetic anisotropy. *J. Appl. Phys.* **2014**, *116*, 113903.
(61) Fullerton, E. E.; Jiang, J.; Bader, S. Hard/soft magnetic heterostructures: model exchange-spring magnets. *J. Magn. Magn. Mater.* **1999**, *200*, 392−404.
(62) Zeng, H.; Li, J.; Liu, J. P.; Wang, Z. L.; Sun, S. Exchange-coupled nanocomposite magnets by nanoparticle self-assembly. *Nature* **2002**, *420*, 395−398.
(63) Nandwana, V.; Chaubey, G. S.; Yano, K.; Rong, C.-b.; Liu, J. P. Bimagnetic nanoparticles with enhanced exchange coupling and energy products. *J. Appl. Phys.* **2009**, *105*, 014303−014303−5.
(64) López-Ortega, A.; Estrader, M.; Salazar-Alvarez, G.; Roca, A. G.; Nogués, J. Applications of exchange coupled bi-magnetic hard/soft and soft/hard magnetic core−shell nanoparticles. *Phys. Rep.* **2015**, *553*, 1−32.
(65) Magno de Lima Alves, T.; Amorim, B. F.; Morales Torres, M. A.; Bezerra, C. G.; Nóbrega de Medeiros, S.; Gastelois, P. L.; Fernandez Outon, L. E.; Augusto de Almeida Macedo, W. Wasp-waisted behavior in magnetic hysteresis curves of $CoFe_2O_4$ nanopowder at a low temperature: experimental evidence and theoretical approach. *RSC Adv.* **2017**, *7*, 22187−22196.
(66) Wang, X.; He, H.; Wang, F.; Chen, Y.; Xu, L.; Li, X.; Zhang, X. Preparation and magnetic properties of anisotropic (Sm,Pr)Co5/Co composite particles. *J. Magn. Magn. Mater.* **2012**, *324*, 889−892.
(67) Pourroy, G.; Viart, N.; Läkamp, S. Magnetic characterization of composites Fe−Co alloy/Co containing magnetite. *J. Magn. Magn. Mater.* **1999**, *203*, 37−40.
(68) Buscaglia, M. T.; Buscaglia, V.; Curecheriu, L.; Postolache, P.; Mitoseriu, L.; Ianculescu, A. C.; Vasile, B. S.; Zhe, Z.; Nanni, P. Fe_2O_3@$BaTiO_3$ Core-Shell Particles as Reactive Precursors for the Preparation of Multifunctional Composites Containing Different Magnetic Phases. *Chem. Mater.* **2010**, *22*, 4740−4748.
(69) Das, R.; Robles, J.; Glassell, M.; Kalappattil, V.; Phan, M. H.; Srikanth, H. Magnetic anisotropy and switching behavior of Fe_3O_4/$CoFe_2O_4$ core−shell nanoparticles. *J. Electron. Mater.* **2019**, *48*, 1461−1466.
(70) Gavrilov-Isaac, V.; Neveu, S.; Dupuis, V.; Taverna, D.; Gloter, A.; Cabuil, V. Synthesis of Trimagnetic Multishell $MnFe_2O_4$@$CoFe_2O_4$@$NiFe_2O_4$ Nanoparticles. *Small* **2015**, *11*, 2614−2618.
(71) Sun, S.; Zeng, H.; Robinson, D. B.; Raoux, S.; Rice, P. M.; Wang, S. X.; Li, G. Monodisperse MFe_2O_4 (M = Fe, Co, Mn) Nanoparticles. *J. Am. Chem. Soc.* **2004**, *126*, 273−279.
(72) Glinka, C. J.; Barker, J. G.; Hammouda, B.; Krueger, S.; Moyer, J. J.; Orts, W. J. The 30 m small-angle neutron scattering instruments at the National Institute of Standards and Technology. *J. Appl. Crystallogr.* **1998**, *31*, 430−445.
(73) Krycka, K.; Jackson, A.; Dennis, C. Magnetic Structure of Iron Oxide Nanoparticles Using SANS. *Summer School on Small Angle Neutron Scattering and Neutron Reflectometry*; NIST, 2010.
(74) Krycka, K. *Python script*. https://github.com/krycket (accessed 2023-06-11).
(75) Doucet, M.; Cho, J. H.; Alina, G.; Bakker, J.; Bouwman, W.; Butler, P.; Campbell, K.; Gonzales, M.; Heenan, R.; Jackson, A., et al. *SasView*, version 4.2.2, 2019. http://www.sasview.org (accessed 2023-06-11).
(76) Ueno, T.; Saito, K.; Yano, M.; Ito, M.; Shoji, T.; Sakuma, N.; Kato, A.; Manabe, A.; Hashimoto, A.; Gilbert, E. P.; Keiderling, U.; Ono, K. Multiple magnetic scattering in small-angle neutron scattering of Nd-Fe-B nanocrystalline magnet. *Sci. Rep.* **2016**, *6*, 28167.
(77) Krycka, K.; Borchers, J.; Ijiri, Y.; Booth, R.; Majetich, S. Polarization-analyzed small-angle neutron scattering. II. Mathematical angular analysis. *J. Appl. Crystallogr.* **2012**, *45*, 554−565.
(78) Moon, R. M.; Riste, T.; Koehler, W. C. Polarization Analysis of Thermal-Neutron Scattering. *Phys. Rev.* **1969**, *181*, 920−931.
(79) *SASView Paracrystal Model*. https://www.sasview.org/docs/user/models/fcc_paracrystal.html (accessed 2023-01-24).
(80) *SASView Raspberry Model*. https://www.sasview.org/docs/user/models/raspberry.html (accessed 2023-01-24).

https://doi.org/10.1021/acsanm.3c00510
ACS Appl. Nano Mater. 2023, 6, 10986−11000